# Behavior of zircon in the upper-amphibolite to granulite facies schist/migmatite transition, Ryoke metamorphic belt, SW Japan: constraints from the melt inclusions in zircon

AUTHOR(S):

Kawakami, Tetsuo; Yamaguchi, Isao; Miyake, Akira; Shibata, Tomoyuki; Maki, Kenshi; Yokoyama, Takaomi D.; Hirata, Takafumi

CITATION:

Kawakami, Tetsuo ...[et al]. Behavior of zircon in the upper-amphibolite to granulite facies schist/migmatite transition, Ryoke metamorphic belt, SW Japan: constraints from the melt inclusions in zircon. Contributions to Mineralogy and Petrology 2013, 165(3): 575-591

ISSUE DATE:

2013-03

URL:

http://hdl.handle.net/2433/172347

# Behavior of zircon in the upper-amphibolite to granulite facies schist/migmatite transition, Ryoke metamorphic belt, SW Japan: Constraints from the melt inclusions in zircon

**Tetsuo KAWAKAMI[1, *], Isao YAMAGUCHI[1], Akira MIYAKE[1], Tomoyuki SHIBATA[2], Kenshi MAKI[1], Takaomi D. YOKOYAMA[1], Takafumi HIRATA[1]**

Published in:
*Contributions to Mineralogy and Petrology (2013)*
*Volume 165, pp.575-591*
*DOI 10.1007/s00410-012-0824-7*

[1] Department of Geology and Mineralogy, Graduate School of Science,
Kyoto University, Kitashirskawa-Oiwake-cho, Sakyo-ku, Kyoto 606-8502, Japan

[2] Institute for Geothermal Sciences, Graduate School of Science,
Kyoto University, Noguchihara, Beppu, Oita 874-0903, Japan

[*]Corresponding author: T. Kawakami, t-kawakami@kueps.kyoto-u.ac.jp
Running title: Melt inclusions in Zrn from migmatites, Ryoke belt, Japan

## Abstract

Behavior of zircon at the schist/migmatite transition is investigated. Syn-metamorphic overgrowth is rare in zircon in schists, whereas zircon in migmatites has rims with low Th/U that give 90.3 ± 2.2 Ma U-Pb concordia age. Between inherited core and the metamorphic rim, a thin, dark-CL annulus containing melt inclusion is commonly developed, suggesting that it formed contemporaneous with the rim in the presence of melt. In diatexites, the annulus is further truncated by the brighter-CL overgrowth, suggesting the resorption and regrowth of the zircon after near-peak metamorphism. Part of the zircon rim crystallized during the solidification of the melt in migmatites.

Preservation of angular-shaped inherited core of 5-10 μm in zircon included in garnet suggests that zircon of this size did not experience resorption but developed overgrowths during near-peak metamorphism. The Ostwald ripening process consuming zircon less than 5-10 μm is required to form new overgrowths. Curved crystal size distribution pattern for fine-grained zircons in a diatexite sample may indicate the contribution of this process. Zircon less than 20 μm is confirmed to be an important sink of Zr in metatexites, and ca. 35 μm zircon without detrital core are common in

diatexites, supporting new nucleation of zircon in migmatites.

In the Ryoke metamorphic belt at the Aoyama area, monazite from migmatites records the prograde growth age of 96.5 ± 1.9 Ma. Using the difference of growth timing of monazite and zircon, the duration of metamorphism higher than the amphibolite facies grade is estimated to be ca. 6 Myr.

Keywords: zircon, migmatite, melt inclusion, glass, crystal size distribution, duration of metamorphism.

## Introduction

Behavior of zircon during the metamorphism is a matter of great interest because zircon could grow during many stages of metamorphism and the U-Pb spot ages of this mineral could constrain the timing of its growth due to the sluggish nature of the Pb diffusion in it (e.g. Harley et al. 2007; Rubatto and Hermann 2007). Microstructural information gives significant constraints on the origin of zircon (Vavra et al. 1996; 1999; Schaltegger et al. 1999; Corfu et al. 2003; Geisler et al. 2007; Rubatto and Hermann 2007; Higashino et al. 2012), so understanding the mechanism of microstructure formation is of great importance. Above all, behavior of zircon at the amphibolite to granulite facies transition is important since the role of partial melting on the growth and microstructure formation of zircon can be understood from such studies (e.g. Schiøtte et al. 1989; Vavra et al. 1999; Bowman et al. 2011). In the polymetamorphic orthogneiss from northern Labrador, Canada, almost no zircon grows in the amphibolite facies gneisses, and it starts to grow near the amphibolite-granulite facies transition (Schiøtte et al. 1989). Vavra et al. (1999) described the zoning pattern of zircon from the amphibolite-granulite facies transition of the Ivrea Zone (Southern Alps) in detail. In the Ivrea Zone, this grade of metasediments accompanies partial melting, and all the zircon overgrowth was supposed to have formed entirely in an anatectic environment. They observed an angular shape of inherited core of zircon in metasediments and interpreted that it is not affected by the partial dissolution process. Since dust-like tiny zircons are abundant in the metasediments, they assumed the Ostwald ripening as a possible growth mechanism of zircon overgrowth, and considered that such a process took place during the prograde metamorphism. They recognized three patterns of zircon overgrowth based on morphology and internal structure as follows; (i) prismatic (prism-blocked) with low Th/U ratio and dark-cathodoluminescence (dark-CL), (ii) stubby with medium Th/U ratio, and (iii) isometric with high Th/U ratio and bright-CL. The former two were observed at amphibolite facies and the latter two was observed at granulite facies. They ascribed prismatic zoning to be due to the growth in amphibolite facies $H_2O$ saturated melt whereas isometric zoning to be due to the growth in granulite facies $H_2O$ undersaturated melt (Vavra et al. 1999).

Recently, melt inclusions are found in migmatites and granulites (Cesare et al. 2003; 2009; 2011).

One of the important host minerals of the melt inclusions is zircon (Cesare et al. 2003). The melt inclusions are the direct evidence of the partial melting, and thus they enable to reliably constrain the timing and environment in which zircon grew. Cesare et al. (2009) reports a garnet porphyroblast that includes a monazite with melt inclusion and a zircon with an euhedral overgrowth. They interpret that zircon growth in an anatectic environment was almost simultaneous with the garnet growth, and occurred early in the melting process (Cesare et al. 2009). However, systematic evaluation of zircon microstructure formed under the amphibolite to granulite facies metamorphism that utilizes melt inclusions to constrain the timing of zircon microstructure formation is not sufficiently available yet.

In this study, zircon in the upper-amphibolite to granulite facies pelitic and psammitic metamorphic rocks of the Ryoke metamorphic belt at the Aoyama area are studied in detail in order to understand the behavior of zircon in the anatectic migmatite front. The presence of melt inclusions in the zircon rims, resorption microstructure of near-peak overgrowth truncated by the later overgrowth, and the result of laser ablation inductively coupled plasma mass spectrometry (LA-ICP-MS) U-Pb dating of zircon in combination with X-ray fluorescence (XRF) and modal analyses show that the zircon rims of the Aoyama area partly grew during the near-peak metamorphism in the presence of melt, and after partial resorption, further overgrowth developed during the retrograde, melt crystallization stage.

Mineral abbreviations are after Kretz (1983).

## Geological outline of the Aoyama area

The Ryoke metamorphic belt shows an elongated distribution over 800 km in SW Japan (Fig. 1a), and is one of the most famous high-temperature, low-pressure type metamorphic belts in the world (Miyashiro 1965; Okudaira et al. 1993; Okudaira 1996; Ikeda 1998a, b; Brown 1998; Nakajima 1994; Suzuki and Adachi 1998; Kawakami and Ikeda 2003; Kawakami 2004). It is mainly composed of pelitic and psammitic metamorphic rocks and metacherts, and the highest grade zones are considered to have reached granulite facies conditions at the metamorphic peak (e.g. Ikeda 2002). The metamorphic belt grades into the unmetamorphosed sedimentary complex of the Mino-Tanba terrane to the north that is mainly made up of Middle to Late Jurassic turbidites and shales (e.g., Wakita 1987).

The Aoyama area is one of the well-studied areas in the Ryoke metamorphic belt, where high-grade metasedimentary rocks are widely exposed (Yoshizawa et al. 1966; Hayama et al. 1982; Takahashi and Nishioka 1994; Kawakami 2001a; Kawakami and Nishioka 2012) (Fig. 1b). The rock facies of the pelitic-psammitic rocks are the schists in the northern half of the area (white part of Fig. 1b), and are anatectic migmatites in the southern half of the area (gray part of Fig. 1b). Migmatites

are mostly metatexite, but diatexite is also common in the southwestern part of the migmatite dominant zone. The chemical Th–U-total Pb isochron method (CHIME) dating of monazite from the migmatites records the prograde monazite growth age of 96.5 ± 1.9 Ma during the regional, Ryoke metamorphism (Kawakami and Suzuki 2011). This is similar to the CHIME monazite age of the Ryoke metamorphic rocks reported from other areas where contact metamorphism by granite intrusion is not significant (e.g. Suzuki and Adachi 1998).

The Kabuto granodiorite and the Ao granite that postdate regional metamorphism intrude discordantly to the foliations of metamorphic rocks in the Aoyama area (Yoshida et al. 1995). The Kabuto granodiorite gives the Rb-Sr-whole-rock age of 79.2 ± 10.2 Ma (Tainosho et al. 1999) and accompanies a contact aureole. The Ao granite gives the CHIME monazite age of 79.8 ± 3.9 Ma (Kawakami and Suzuki 2011). Monazite from the migmatite zone widely records 83.5 ± 2.4 Ma thermal event in addition to the 96.5 ± 1.9 Ma age (Kawakami and Suzuki 2011) although the contact aureole is not evident from the major metamorphic mineral assemblage (Takahashi and Nishioka 1994). Kawakami and Suzuki (2011) attributed 83.5 ± 2.4 Ma overprint to the thermal effect and monazite-fluid interaction caused by the intrusion of the Ao granite and the Kabuto granodiorite.

The Aoyama area is previously divided into two regional metamorphic zones and one contact metamorphic zone, utilizing mineral assemblages in pelitic lithology (Kawakami 2001a). The regional metamorphic zones in the order of increasing metamorphic grade are (i) Sil-Kfs zone, where Ms + Qtz is unstable and Sil + Kfs + Bt is stable, and (ii) Grt-Crd zone, where Grt + Crd + Bt ± Sil is stable. The contact metamorphic zone is recognized by the occurrence of Grt + Crd assemblage in the granodiorite side (Fig. 1b). The peak pressure-temperature (*P-T)* conditions are estimated to be 3.0-4.0 kbar, 615-670 $^{o}$C for the Sil-Kfs zone, and 4.5-6.0 kbar, 650-800 $^{o}$C for the Grt-Crd zone (Kawakami 2001a). These estimates are based on the Grt-Bt geothermometers and GASP geobarometers, possibly giving the lowest temperature estimates due to the retrograde re-equilibrium between garnet and biotite. High spessartine content in the garnet from the schist-dominant part of the Grt-Crd zone suggests that introduction of MnO into garnet stabilized the Grt + Crd assemblage even under the lower temperature condition than the petrogenetic grid for the KFMASH system predicts (Kawakami, 2001b). A pseudosection of Wei et al. (2004) constructed for KMnFMASH + quartz system using typical pelite composition ($M_{Mn}$ = Mn/(Mn+Fe+Mg) = 0.007) of Mahar et al. (1997) shows that increase of $M_{Mn}$ widens the stability field of Grt + Crd assemblage very much. With $M_{Mn}$ = 0.03, it is stable in subsolidus field even at 2 kbar, 650 $^{o}$C. This is consistent with the whole-rock Mn content of pelitic metamorphic rocks in the Aoyama area having a $M_{Mn}$ value up to 0.03 (Kawakami 2001b) and with the field observation that Grt + Crd assemblage is found not only in migmatite-dominant area but also in the schist-dominant area. Therefore, effect of Mn is probably responsible for the low-temperature estimates for the Grt + Crd bearing samples in

the Aoyama area.

In the Grt-Crd zone, dehydration melting reaction such as

$$Bt + Sil + Qtz = Crd \pm Kfs + melt \quad (1)$$

and

$$Bt + Sil + Qtz = Grt + Crd \pm Kfs \pm Ilm + melt \quad (2)$$

are responsible for the formation of migmatites (Kawakami 2001a, b).

Besides the Grt-Crd isograd that is subparallel to the schist/migmatite lithological boundary, a line marking the breakdown of tourmaline was mapped and termed the 'tourmaline-out isograd' (Kawakami 2001a, 2004). This isograd is further extended to the western side of the Aoyama area in the present study (Fig. 1b). Near this isograd, magmatic andalusite is locally found, based on which nearly isothermal decompression *P-T* path was proposed for the Grt-Crd zone (Kawakami 2002). Melt extraction of 12–14 wt.% from the migmatite zone is estimated in the Aoyama area (Kawakami and Kobayashi 2006).

## Sample description and methodology

Samples used in this study are from the Grt-Crd zone where lithological change from schist to migmatite as a function of increasing metamorphic grade can be observed (Fig. 1b). Three pelitic and psammitic schists, 13 metatexites and 4 diatexites were collected (Fig. 1b). Mineral assemblage and other details of the samples used in this study are summarized in Table 1.

These samples were prepared as polished thin section for the electron microprobe analysis of constituting minerals and modal analysis of zircon. Remaining halves of the rock chips used for thin sectioning (i.e., the same area with a thin section, ca. 5 mm thickness) were powdered, and utilized in the trace element analysis by the XRF spectrometer Rigaku 3070 (Goto and Tatsumi 1996) at the Geothermal Research Institute, Kyoto University. The migmatite sample is chemically banded and the distribution of zircon within a sample is heterogeneous to some extent. In order to minimize such effect in comparing zircon mode and whole-rock Zr content, using 'the same system size' is preferable. This is why the remaining halves of the rock chips used for thin sectioning were utilized in the determination of whole-rock Zr concentration.

Zircon grains in the thin section were observed under the SEM-EDS (Hitachi S-3500H equipped with EDAX X-ray analytical system) and JEOL JXA8105 superprobe using back scattered electron (BSE) images, qualitative analysis and an X-ray imaging. Size of zircon (major and minor axes) whose major axis is more than 20 μm (written as 'zircon (> 20 μm)' hereafter) was measured using BSE image of WDS. Zircon (< 20 μm) was not counted nor measured because they are so common and it is difficult not to overlook them. Using this grain size data of zircon (> 20 μm), crystal size distributions (CSDs) were calculated and CSD plots were constructed for each sample, following

Cashman and Ferry (1988) and Morishita (1992). The number of zircon crystals per size class and per unit volume (Nv) is represented by Nv = $(c/a)^{1.5}/\Delta L$ (Cashman and Ferry 1988; Moroshita 1992), where $c$, $a$ and $\Delta L$ are the number of zircon crystals within the size class, measured area (whole thin section in this study), and the size class (5 μm in this study).

Modal amount of zircon (> 20 μm) was determined using the BSE images as follows:

Modal amount of zircon (> 20 μm)
= (Sum of the area of zircon (> 20 μm) in a thin section)/(area of whole thin section),

where area of each zircon grain was calculated in two ways; assuming ellipsoidal shape of zircon grains or rectangular shape of them (Table 1). The latter gives the possible maximum modal amount of zircon.

The X-ray elemental mapping of whole thin section was performed for the sample AN44, in order to determine the CSD plot of zircon covering zircon (< 20 μm). The beam diameter was 3 μm and the step for the mapping was 5μm each. The grain size of zircon was determined using the elemental map of Zr and 'analyze particles' function of the ImageJ software. Feret's diameter of each grain calculated by ImageJ software was used to determine the CSD of zircon. Comparison of this CSD with the CSD data obtained by the modal counting of zircon enabled to convert the apparent grain size obtained by the elemental mapping to the real grain size.

Zircon grains in selected schist and migmatite samples from the Grt-Crd zone (Table 1) were utilized in U-Pb dating using a Nu AttoM single-collector ICP-MS coupled to a NWR-193 laser-ablation system utilizing a 193 nm ArF excimer laser at Kyoto University. The zircon dating was performed *in situ* on polished thin sections after BSE and CL image observations. Instrumental parameters are listed in Table 2. The laser was operated with output energy of ~ 4.4 mJ per pulse, repetition rate of 6 Hz and laser spot size of 20 μm in diameter, providing an estimated power density of the sample of 1.60-2.23 J/cm$^2$. The pulse count was 100 shots. The ablation occurs in He gas within the sample cell, and then the ablated sample aerosol and He gas were mixed with Ar gas downstream of the cell. He minimizes redisposition of ejecta or condensates while Ar provides efficient sample transport to the ICP-MS (Eggins et al. 1998; Gunther and Heinrich 1999; Jackson et al. 2004). The signal-smoothing device was applied to minimize the introduction of large aerosols into the ICP, reducing signal spikes (Tunheng and Hirata 2004).

The ICP-MS is optimized using continuous ablation of a 91500 zircon standard (Wiedenbeck et al. 1995; 2004) and NIST SRM 610 to provide maximum sensitivity. Data were acquired on seven isotopes, $^{202}$Hg, $^{204}$Pb, $^{206}$Pb, $^{207}$Pb, $^{208}$Pb, $^{232}$Th, and $^{238}$U using a peak jumping acquisition mode, which measures the signal intensity at the peak top.

Background and ablation data for each analysis were collected over 150 and 11 seconds, respectively. Backgrounds were measured with the laser shutter closed and employing identical settings and gas flows to those used during ablation. Data were acquired consisting of multiple

groups of 10 sample unknowns bracketed by quartets of NIST SRM 610 and 91500 zircon standards (Wiedenbeck et al, 1995; 2004), which are sandwiched by a background analysis.

$^{202}$Hg was monitored to correct the isobaric interference of $^{204}$Hg on $^{204}$Pb. To reduce the isobaric interference, an Hg-trap device with an activated charcoal filter was applied to the Ar make-up gas before mixing with He carrier gas (Hirata et al. 2005). Prior to each individual analysis, regions of interest were pre-ablated using a pulse of the laser with a spot size of 35 μm in diameter to remove potential surface contamination, dramatically reducing common Pb contamination (Iizuka and Hirata 2004). The average 204 intensities of background and samples for all the analysis performed in this study are 7680 cps and 7725 cps, respectively (average 204 intensity of selected analysis shown in Table 3 is 7690 cps). Most of 204 intensity for background is Hg, as indicated by a background $^{202}$Hg/204 ratio indistinguishable from natural Hg, $^{202}$Hg/$^{204}$Hg = 29.863/6.865. When $^{204}$Pb data for unknown sample was obtained and a sample has a discordant age without common Pb correction, common Pb correction was applied to the sample following the two-stage model of Stacey and Kramers (1975). The maximum level of the correction was fourth time. If the sample required more than the maximum level of correction, the age of sample was discarded. The effect of the common Pb correction was factored into the analytical errors on the ages.

All data reduction including the common Pb correction was conducted off-line using in-house Excel spreadsheet. Background intensities were interpolated using an averaged value among four background data acquired before and after the each unknown sample groups. The mean and standard deviation of the measured ratios among each eight NIST SRM 610 and 91500 zircon standard data bracketing unknown sample groups were calculated, and the mean and standard deviation measured for 91500 zircon standard were applied for age estimate and uncertainty propagation. All uncertainties are quoted at the 2 sigma level. $^{235}$U was calculated from $^{238}$U using a $^{238}$U/$^{235}$U ratio of 137.88 (Jaffey et al. 1971).

Inclusions phases in zircon grains were observed using JEOL FE-SEM at Osaka University and transmitted electron microscope (TEM) Hitachi H8000k equipped with KEVEX EDS system at Kyoto University. The TEM samples were prepared from the polished thin sections using focused ion beam (FIB) FEI Quanta 200 3DS at Kyoto University.

## Results

### Modal amount of zircon and whole-rock Zr concentration

The modal analysis of zircon (> 20 μm) was performed on 11 pelitic and psammitic schists, metatexite and diatexite samples (Fig. 1b, Table 1). Figure 2 is a diagram showing the relationship between the whole-rock Zr content and the modal amount of zircon (> 20 μm). Comparing the

modal amount of zircon (> 20 μm) in schists, metatexites and diatexites having almost the same whole-rock Zr content around 170-190 ppm, there is a tendency that the modal amount of zircon (> 20 μm) is higher in the schists than the metatexites, and diatexites are in between them (Fig. 2). About 60% of the whole-rock Zr is hosted in zircon (> 20 μm) in schists, but zircon (> 20 μm) hosts less than 40% of whole-rock Zr in metatexites. In diatexites, 30-50% of the whole-rock Zr is hosted in zircon (> 20 μm).

Figure 3 is a plot showing a grain size distribution of zircon determined by an X-ray elemental mapping of a whole thin section of a metatexite sample AN44. Open diamonds are plotted using Feret's diameter determined by the elemental mapping and the ImageJ software. This diameter could be affected by step sizes and beam diameter of the elemental mapping. Grain size of the gray squares was determined under BSE observation, and thus considered reliable. The major axis of zircon is used as a grain size in this study. These two methods gave different, but almost parallel, linear least squares fit lines (Fig. 3). Since these two should be identical, and subtraction of 8 μm from the grain sizes determined by the elemental mapping (solid triangles in Fig. 3) results in good coincidence between the two (solid and dotted lines), we consider that the grain size distribution of the sample AN44 covering all the zircon size range could be approximately represented by the solid triangle data (Fig. 3).

Figure 4 is the summary of CSD plots for 2 schist samples (Fig. 4a, b), 4 metatexites (Fig. 4c-f), and 4 diatexites (Fig. 4g-k). There is a tendency that the CSD plots of the grain size range of 25-40 μm commonly define a linear trend. It is rarely curved at the smallest grain size range (20-35 μm) in sample Y32A. Data for coarse-grained zircons in the plot (more than 40-50 μm size in most cases) tend to be discordant with the least squares fit lines (e.g., Fig. 4a, e-f, i-j), possibly due to the small grain numbers (1 to 3).

## Zircon in diatexites of the Grt-Crd zone

Zircon in the garnet-free diatexites from the Grt-Crd zone, especially those containing abundant coarse-grained zircon grains, clearly shows the core-rim microstructure; core is the inherited part from the protolith showing various ages (Fig. 5) and the rim overgrowths develop on it. The core-rim boundary can be commonly identified by the presence of characteristic thin, dark-CL (bright BSE) annulus (Fig. 5a-l, o-r, w-x). Although the dark annulus itself cannot be dated because it is too thin, ubiquitous occurrence of it at the immediate contact between inherited core and the rim regardless of the variety of the inherited core ages (Fig. 5) suggests that the dark-CL annulus is contemporaneous with the rim overgrowth, and formed during the latest metamorphic event, that is, the Ryoke metamorphism. The dark-CL annulus commonly includes tiny, dark inclusions of less than several microns in diameter (Fig. 5a-l, o-r, w-x). Such inclusions are abundant in pyramid faces where

289 overgrowth is thicker and probably faster (Fig. 5c-d, i-j). This microstructure resembles very much
290 with that observed in zircons from the El Hoyazo enclave (Cesare et al. 2003). In the case of El
291 Hoyazo, one of the tiny inclusions was confirmed to be a rhyolitic glass.
292 In order to confirm the presence of melt inclusions in our sample, tiny inclusions present in the
293 dark-CL annulus of zircon were prepared for the TEM observation utilizing FIB. Figure 6 shows the
294 bright and dark field images of the sample G6 and the electron diffraction patterns of the inclusions
295 in it. Judging from the diffuse, halo pattern of the electron diffraction images, inclusions 1, 3 and 5
296 are the glass, and inclusions 2 and 4 are the mixture of glass and crystal. The EDS analysis under
297 TEM and FE-SEM shows that inclusion 3 is a glass containing K, Al and Si, and inclusion 1 is a
298 Si-rich glass. The melt inclusions rarely have pores (inclusion 2 of Fig. 6) that resembles to the
299 'micro- to nano-porosities' (terminology after Cesare et al. 2011) reported from nanogranites.
300 Presence of pores and daughter crystals in the glass inclusions in zircon is also observed in plutonic
301 rocks (Thomas et al. 2003).
302 The core of the zircon is often oscillatory zoned both in CL and BSE images and such a zoning is
303 truncated by the rim overgrowth (Fig. 5a-b, e-f, k-l). The shape of the core (inside of the dark-CL
304 annulus) is often angular (Fig. 5a-b, i-j), as observed in the case of metapelites from the amphibolite
305 and granulite facies transition in Ivrea Zone (Vavra et al. 1999), but the rounded ones are also
306 present (Fig. 5o-r). The important characteristic of the dark-CL annulus in the garnet-free diatexite
307 zircon is that it varies in thickness and commonly truncated by the lighter-colored overgrowth (Fig.
308 5a-b, g-h, w-x).
309 Zircon grains without the inherited core are not uncommon in the matrix and the grain size is ca.
310 35 μm (Fig. 5m-n), both in garnet-free and garnet-bearing diatexites. They show rounded shape and
311 lack zoning, and show similar CL brightness with the bright-CL overgrowth developed at the coarse
312 zircon rim. They also lack the dark-CL annulus. Based on transmitted light microscope observation,
313 some of them are the rim of the coarse grained zircon. However, common occurrence of ca. 35 μm
314 grains with young ages as reported below supports that some of them are newly nucleated ones
315 contemporaneous with the coarse-grained zircon rims.
316 Zircon with dark-CL annulus and tiny inclusion alignments are also found in the matrix and as
317 inclusions in garnet from the garnet-bearing diatexite. In a garnet-bearing diatexite sample G11,
318 major axis of zircon (> 20 μm) is mostly 20-30 μm (Fig. 4h) and the dark-CL annulus and tiny
319 inclusion alignments are rarely observed in the matrix zircon (Fig. 5o-p, s-x). Zircon inclusion in
320 garnet often has a major axis less than 30 μm (Fig. 5q-r), and has dark-CL annulus and tiny inclusion
321 alignment. Most of the matrix zircon lacks apparent inherited core, and their microstructure and
322 CL-intensity resemble to the possible newly nucleated grains observed in the garnet-free diatexites
323 (Fig. 5m-n). Some matrix zircon grains show dark-CL annulus truncated by the overgrowth rim (Fig.
324 5w-x) as in the case of garnet-free diatexites. Although it is still not clear whether this

microstructural difference between garnet-free and garnet-bearing diatexites are common in other diatexites in the Aoyama area or not, the important observation in this study is that both zircon rim overgrowth and newly crystallized grains can be recognized in garnet-free and garnet-bearing diatexites, and zircon in these diatexites also share the characteristic that dark-CL annulus is further truncated by the overgrown rim.

The LA-ICP-MS U-Pb dating of zircon rims and the grains without inherited cores give the concordia age of ca. 90.3 ± 2.2 Ma (Fig. 7b). The cores give concordant ages of ca. 2100-1700 Ma, ca. 550 Ma and ca. 250-120 Ma, and these are considered to be inherited, detrital ages (Fig. 7a). Most of the rim overgrowths were too thin for the LA-ICP-MS U-Pb dating with 20 μm spot-size, so that many mixed analyses of inherited core and rim resulted in the formation of discordia in the concordia diagram (Fig. 7a). The Th/U ratio of the zircon core varies while that of the 90.3 ± 2.2 Ma rim is very low, mostly below 0.02 (Table 3).

**Zircon in schists and metatexites of the Grt-Crd zone**

Zircon in pelitic and psammitic schist of the Grt-Crd zone is found in the matrix, and intimate microstructural correlation between other mineral such as biotite is not observed. Microstructure of zircon does not differ between the pelitic and psammitic lithology, and the dark-CL annulus developed on the inherited core, accompanied by the inclusions similar to diatexite zircons, is rarely observed (Fig. 8). Rim overgrowth, if present, is about several microns in thickness (Fig. 8c-h, k-l, o-v). Zircon grains that do not have rim overgrowth are also common (Fig. 8a-b, m-n). Even in such cases, inclusion alignments are found along the healed cracks that can be observed in CL images (Fig. 8k-l). Shape of the core is often angular (Fig. 8e-h, k-l, q-r, u-v), although rounded variety is also present.

Zircon in metatexite is found in the matrix (Fig. 9e-h, k-t), as well as inclusions in garnet porphyroblasts (Fig. 9a-b, i-j) or biotite (Fig. 9m-n). Zircon in the matrix is commonly found adjacent to biotite or quartz in mesosome and melanosome. It is rare in leucosome. The dark-CL annulus with inclusions is developed in most of the zircon grains found in the matrix (Fig. 9e-h, k-t). Nanogranite-like polyphase inclusion is included in the dark-CL annulus of zircon grain AN07a-7 (Fig. 9o-p). The dark-CL annulus is further overgrown by the brighter-CL overgrowth (Fig. 9e-h, k-t). The thickness of the rim overgrowth is, in most cases, less than 10 μm. Shape of the core is often angular (Fig. 9e-f, k-l, q-r), even if the zircon is included in garnet (Fig. 9i-j), although rounded variety is also common (Fig. 9m-n).

Zircon inclusions in garnet porphyroblast are often less than 20 μm, with or without core-rim microstructure (Fig. 9a-b, i-j). Monazite is also included in the same garnet, so monazite and zircon coexisted during the near-peak metamorphism when garnet grew. An example of inclusion zircon

from sample AN07 has angular-shaped core, overgrown by the dark-CL annulus and brighter-CL overgrowth on it (Fig. 9i-j). Dark-CL annulus has many inclusions of unidentified phases less than several microns in diameter (Fig. 9i-j, shown by arrows), microstructure of which resembles very much to the zircon with melt inclusions found in diatexites (Fig. 5). Different from diatexites, the dark-CL annulus is not truncated by the brighter-CL overgrowths in most of the metatexite samples (Fig. 9).

The dark-CL annulus and brighter-CL overgrowth on zircon in schists and metatexites are thinner than the spot size (20 μm) of the LA-ICP-MS U-Pb dating. Because of this, most dating on the zircon rim could be only done as mixtures with the inherited core. The result is plotted on a concordia diagram (Fig. 10). Most results are lying on a discordia, which is actually a mixing line resulted from the mixed analysis of the core and rim. The inferred lower intercept around ca. 90 Ma implies the presence of the rim overgrowth of ca. 90 Ma (Fig. 10). A zircon grain from the metatexite (sample AN52) with characteristic core-rim microstructure gave near-concordant age of 115 ± 6.0 Ma and relatively low Th/U ratio of 0.16 (Fig. 9g-h). Presence of this kind of mixed age also supports the growth of young zircon rim in metatexites. Therefore, the thin zircon rim observed in the schists and metatexites is probably identical to the 90.3 ± 2.2 Ma zircon rim observed in diatexites. The cores of zircon from schists and metatexites give concordant U-Pb ages of ca. 2500 Ma, ca. 2200-1700 Ma, ca. 600 Ma and ca. 230-120 Ma, and these are considered to be inherited, detrital ages (Fig. 10).

## Discussion

### Behavior of zircon at the schist-migmatite transition of the Aoyama area

#### Mechanism of zircon growth in the Aoyama area

The modal amount of zircon (> 20 μm) is high in schists of the Grt-Crd zone, and is lower in metatexites (Fig. 2). This tendency is not controlled by the difference in the whole-rock Zr concentration, because it is observed for the schists and metatexites showing similar whole-rock Zr concentration (Table 1, Fig. 2). Figure 2 shows that about 60% of the whole-rock Zr is contained in zircon (> 20 μm) in the schists, whereas less than 40% of the whole-rock Zr is contained in zircon (> 20 μm) in metatexites. In diatexites, 30-50% of whole-rock Zr can be accounted for by the presence of zircon (> 20 μm), which is higher than the metatexites case. From the CSD plot of the metatexite sample AN44 (Fig. 3), abundant occurrence of fine-grained zircon (< 20 μm) is confirmed, and from a modal amount calculation of fine-grained zircon, roughly 20-40% of whole-rock Zr resides in zircon (< 20 μm), assuming rounded shape of them. This suggests that tiny zircon grains are the

397 important carrier of whole-rock Zr.

398 Angular shape of the core of zircon in metatexites and diatexites (Figs. 5a-b, i-j, 9e-f, k-l, q-r)
399 suggests that these cores did not resorb (Vavra et al. 1999), and the rim grew without experiencing
400 resorption. Since the zircon included in peritectic garnet has tiny inclusion alignment and dark-CL
401 annulus that resemble to melt-inclusion-bearing zircon in diatexites, the rim overgrowth on angular
402 core probably occurred in the presence of melt.

403 The source of Zr for this rim overgrowth is problematic. One possible source of Zr required for
404 the rim overgrowth is the breakdown of Zr-bearing phases other than zircon. Biotite is not an
405 important sink of Zr (Bea et al. 2006), and thus biotite breakdown cannot supply sufficient Zr. The
406 Zr-bearing phases like garnet (Fraser et al. 1997) and ilmenite (Bingen et al. 2001) are the product of
407 the partial melting reaction (2) rather than the reactant, so they cannot provide Zr, either. Minor
408 xenotime (Bea et al. 2006) can be a Zr source for zircon overgrowth, but the microstructural
409 evidence for this is absent so far. Therefore, breakdown of Zr-bearing phases other than zircon is less
410 likely.

411 Accepting that Zr is mostly hosted in zircon (Fraser et al. 1997), and because tiny zircon grains
412 are confirmed to be an important carrier of Zr in samples of this study (Figs. 3, 4), behavior of tiny
413 zircon grains is a key to understand the mechanism of zircon growth. Because the inherited core of
414 zircon in metatexites and diatexites often exceeds 5-10 μm, it is possible that zircon grains less than
415 this size were selectively dissolved through the Ostwald ripening process in the presence of melt at
416 the initial stage of zircon growth (e.g. Vavra et al. 1999). Microstructural observation requests this
417 process if the Zr is not introduced externally, although the observed CSD pattern does not directly
418 support this process. However, the CSD pattern does not deny the Ostwald ripening at the initial
419 stage of zircon growth, since our data does not cover the fine-grained zircon population as 5-10 μm
420 size except for Fig. 3, and the evidence for an early stage process in CSD pattern could be erased by
421 the later processes (e.g. Cashman and Ferry 1988). Judging from the fact that zircon inclusion in
422 peritectic garnet also has an overgrowth accompanying dark-CL annulus and tiny inclusions, this
423 process took place during the near-peak metamorphism.

424 The linear CSD plots generally suggest the continuous nucleation and growth of zircon grains
425 during metamorphism (e.g. Cashman and Ferry 1988; Okudaira 1996). However, as is clear from
426 microstructural observation and LA-ICP-MS dating of zircon, inherited cores are abundant in zircon
427 (Figs. 5, 8, 9). Therefore, theories and interpretation valid for crystals without inherited cores should
428 not be applied directly to this study. A linear CSD trend is even observed for the pelitic schist sample
429 AN24, in which development of zircon overgrowth is not evident (Fig. 8q-v). Therefore, it is highly
430 possible that this linear CSD trend was already acquired at the protolith stage.

431 However, the ca. 35 μm zircon grains with ca. 90 Ma age (Fig. 5m-n), probably representing
432 newly nucleated grains, are common in diatexites. Therefore, fine-grained portion of the CSD plots

for diatexites, at least, could potentially represent the mechanism of zircon growth during the Ryoke metamorphism. The CSD plots of diatexite sample Y32A (Fig. 4h) shows curved nature at the finest grain size range (< 35 μm). This could represent the later modification of originally linear CSD pattern by the Ostwald ripening process (Cashman and Ferry 1988). Therefore, we consider that growth of zircon grains at the near-peak metamorphic stage occurred through the Ostwald ripening process consuming finer-grained zircon than ca. 35 μm in the diatexite sample Y32A.

## Interpretation of the dark-CL annulus and melt inclusions

Zircon (> 20 μm) in the schists is inherited, detrital grain that is evident from the LA-ICP-MS U-Pb zircon dating giving various old ages (Fig. 8). Cretaceous overgrowth on them is very thin or almost absent. However in metatexites, young-aged overgrowth (ca. 90 Ma) is developed in most of the zircon grains as suggested by the presence of zircon rim with similar microstructural characteristics to melt-inclusion-bearing diatexite zircon (Fig. 9), and by the presence of ca. 90 Ma lower intercept for mixed analysis of zircon core and rim (Fig. 10). The ca. 90 Ma rim is commonly separated from the inherited, detrital core by the melt inclusion alignments included in a thin, dark annulus observed under the CL image (Figs. 5, 9). This trend is much clear in diatexites. Since dark-CL annulus is commonly developed on the inherited core of various ages, it is not contemporaneous with the inherited core, but is rather a part of an overgrowth contemporaneous with the ca. 90 Ma rim.

This kind of dark-CL overgrowth on the inherited core of the Ivrea Zone is considered to have formed during the amphibolite facies metamorphism (Vavra et al. 1999). In the Aoyama area, garnet porphyroblasts in metatexites and diatexites include zircon (< 20 μm) with microstructure very similar to the melt-inclusion-bearing dark-CL annulus (Figs. 5, 9). Since garnet is considered to be a product of near-peak metamorphism, this clearly shows that melt inclusions, dark-CL annulus and part of the brighter-CL overgrowth on the dark-CL annulus (all found in zircon inclusions in garnet) are all formed at the near-peak metamorphism. Cesare et al. (2009) also interprets the zircon with euhedral overgrowths included in garnet from El Hoyazo to have formed early in the melting process.

However, this dark-CL annulus is commonly truncated by the bright-CL overgrowth in diatexites (Fig. 5a-b). Therefore, resorption of relatively coarse-grained zircon took place after the near-peak growth of zircon. Such a resorption can occur when the amount of melt increased and the fine-grained zircon was totally consumed. Resorption of zircon continues as far as the amount of melt increases, but it starts to crystallize when the melt starts to cool and crystallize and the solubility of Zr in the melt decreases. Therefore, timing of the bright-CL overgrowth development that truncates dark-CL annulus is the retrograde, melt crystallization stage.

To summarize, zircon rim overgrowth (the dark-CL annulus and an outer part than it) is partly near-peak metamorphic in origin, and partly retrograde. Therefore, the U-Pb ages for zircon rims and newly nucleated grains obtained in this study represent the mixed age of near-peak and retrograde zircons, although the contribution of the near-peak zircon is small in some cases. For example, the analysis spot giving 90 ± 8 Ma in Fig. 5a-b is completely retrograde in origin because the rim analyzed truncates both the dark-CL annulus and part of the bright-CL overgrowth on it. The timing of this zircon rim crystallization is dated to be 90.3 ± 2.2 Ma (Table 3, Fig. 7b). The low Th/U ratio of these young zircon rims (Fig. 5, Table 3) would be due to the coexistence with monazite during its growth (Kawakami and Suzuki 2011; Cesare et al. 2003), as shown by the presence of monazite and zircon with rim overgrowth included in garnet.

A fluid activity during the contact metamorphic event at 83.5 ± 2.4 Ma detected by the CHIME monazite dating is considered responsible for the rejuvenation of the monazite age (Kawakami and Suzuki 2011). Absence of further young overgrowth or rejuvenated part in zircon suggests that zircon was almost immune from the contact metamorphic event at 83.5 ± 2.4 Ma (Kawakami and Suzuki 2011). Overall discussion above suggests that presence of the melt is playing an important role in zircon formation during the high-temperature metamorphism (e.g. Vavra et al. 1999; Rubatto et al. 2001) in the Ryoke metamorphic belt at the Aoyama area.

## Duration of the high-temperature, low-pressure type Ryoke metamorphism

Monazite in the Ryoke metamorphic belt has been considered to record the timing of prograde growth when the rock first attained 525 $^{o}$C (e.g. Suzuki and Adachi 1998). We follow their interpretation that the CHIME monazite age of 96.5 ± 1.9 Ma in the Aoyama area (Kawakami and Suzuki 2011) represents the timing of monazite growth at around 525 $^{o}$C. On the other hand, zircon rims and newly nucleated grains give the mixed age of the near-peak metamorphism to the retrograde, melt crystallization stage (90.3 ± 2.2 Ma; Fig. 7b). The retrograde crystallization of zircon can be the same as or younger than this age. Therefore, using the difference of growth timing of monazite and zircon in the Aoyama area, duration of metamorphism higher than the amphibolite facies grade could be estimated (Fig. 11). These give the duration of high-temperature, low-pressure type Ryoke metamorphism of at least ca. 6 Myr in the case of the Aoyama area. This is a little longer than the estimate of Suzuki et al. (1994) who considered the duration of the Ryoke metamorphism above ca. 500 $^{o}$C to be about 5 Myr.

## Acknowledgements

We would like to thank Takamoto Okudaira and Bernardo Cesare for constructive reviews and

Timothy L. Grove for editorial efforts. Thanks are also due to Fumiko Higashino and Takao Hirajima for LA-ICP-MS analysis, and Akira Tsuchiyama and Toru Matsumoto for FE-SEM analysis. This study was supported by the Grant-in-Aid for Young Scientists (B) (23740391, Tetsuo Kawakami) and Grant-in-Aid for Scientific Research (A) (22244067, Takao Hirajima) from JSPS and MEXT.

## References

Bea, F, Montero, P, Ortega, M (2006) A LA-ICP-MS evaluation of Zr reservoirs in common crustal rocks: Implications for Zr and Hf geochemistry, and zircon-forming processes. The Canadian Mineralogist 44: 693-714

Bingen, B, Austraheim H, Whitehouse M (2001) Ilmenite as a source for zirconium during high-grade metamorphism? Textural evidence from the Caledonides of Western Norway and implications for zircon geochronology. Journal of Petrology 42: 355-375

Bowman JR, Moser DE, Valley JW, Wooden JL, Kita NT, Mazdab FK (2011) Zircon U-Pb isotope, $\delta^{18}O$ and trace element response to 80 m.y. of high temperature metamorphism in the lower crust; sluggish diffusion and new records of Archean craton formation. American Journal of Science 311: 719-772

Brown M (1998) Unpairing metamorphic belts: P-T paths and a tectonic model for the Ryoke Belt, southwest Japan. Journal of Metamorphic Geology 16: 3-22

Cashman KV, Ferry JM (1988) Crystal size distribution (CSD) in rocks and kinetics and dynamics of crystallization. Contributions to Mineralogy and Petrology 99: 401-415

Cesare B, Acosta-Vigil A, Ferrero S, Bartoli O (2011) Melt inclusions in migmatites and granulites. Journal of the Virtual Explorer 38: paper 2, doi: 10.3809/jvirtex.2011.00268

Cesare B, Gomez-Pugnaire MT, Rubatto D (2003) Residence time of S-type anatectic magmas beneath the Neogene Volcanic Province of SE Spain: a zircon and monazite SHRIMP study. Contributions to Mineralogy and Petrology: 146 28-43

Cesare B, Rubatto D, Go´mez-Pugnaire MT (2009) Do extrusion ages reflect magma generation processes at depth? An example from the Neogene Volcanic Province of SE Spain. Contributions to Mineralogy and Petrology 157: 267-279

Corfu F, Hanchar JM, Hoskin PWO, Kinny P (2003) Atlas of zircon textures. Reviews in Mineralogy and Geochemistry 53: 469-500

Eggins SM, Kinsley LPJ, Shelley JMG (1998) Deposition and element fractionation processes during atmospheric pressure laser sampling for analysis by ICP-MS. Applied Surface Science 129: 278-286

Fraser G, Ellis D, Eggins S (1997) Zirconium abundance in granulite-facies minerals, with implications for zircon geochronology in high-grade rocks. Geology 25: 607-610

541 Geisler T, Schaltegger U, Tomaschek F (2007) Re-equilibration of zircon in aqueous fluids and melts.
542 Elements 3: 43-50
543 Goto A, Tatsumi Y (1996) Quantitative analysis of rock samples by an X-ray fluorescence
544 spectrometer (II). Rigaku Journal 13: 20- 38
545 Gunther D, Heinrich CA (1999) Enhanced sensitivity in laser ablation-ICP mass spectorometry using
546 He-Ar mixtures as aerosol carrier. Journal of Analytical Atomic Spectrometry 14: 1363-1368
547 Harley SL, Kelly NM, Moller A (2007) Zircon behaviour and thermal histories of mountain chains.
548 Elements 3: 25-40
549 Hayama Y, Yamada T, Ito M, Kutsukake T, Masaoka K, Miyakawa K, Mochizuki Y, Nakai Y,
550 Tainosho Y, Yoshida M, Kawarabayashi I, Tsumura Y (1982) Geology of the Ryoke Belt in the
551 eastern Kinki District, Japan -The phase-divisions and the mutual relations of the granitic rocks-.
552 Journal of the Geological Society of Japan 88: 451-466 (in Japanese with English abstract)
553 Higashino F, Kawakami T, Satish-Kumar M, Ishikawa M, Maki K, Tsuchiya N, Grantham G, Hirata
554 T (2012) Chlorine-rich fluid or melt activity during granulite facies metamorphism in the Late
555 Proterozoic to Cambrian continental collision zone – an example from the Sør Rondane
556 Mountains, East Antarctica. Precambrian Research *in press*
557 Hirata T, Iizuka T, Orihashi Y (2005) Reduction of mercury background on ICP-mass spectrometry
558 for in situ U-Pb age determinations of zircon samples. Journal of Analytical Atomic
559 Spectrometry 20: 696-701
560 Iizuka T, Hirata T (2004) Simultaneous determinations of U-Pb age and REE abundances for zircons
561 using ArF excimer laser ablation-ICPMS. Geochemical Journal 38: 229-241
562 Ikeda T (1998a) Progressive sequence of reactions of the Ryoke metamorphism in the Yanai district,
563 southwest Japan: the formation of cordierite. Journal of Metamorphic Geology 16: 39-52
564 Ikeda T (1998b) Phase equilibria and the pressure-temperature path of the highest-grade Ryoke
565 metamorphic rocks in the Yanai district, SW Japan. Contributions to Mineralogy and Petrology
566 132: 321-335
567 Ikeda T (2002) Regional occurrence of orthopyroxene-bearing basic rocks in the Yanai district, SW
568 Japan: evidence for granulite-facies Ryoke metamorphism. Island Arc 11: 185-192
569 Jackson SE, Pearson NJ, Griffin WL Belousova EA (2004) The application of laser
570 ablation-inductively coupled plasma-mass spectrometry to in situ U-Pb zircon geochronology.
571 Chemical Geology 211: 47-69
572 Jaffey AH, Flynn KF, Glendenin LE, Bentleyt WC, Essling AM (1971) Precision measurement of
573 half-lives and specific activities of $^{235}$U and $^{238}$U. Physical Review C 4: 1889-1906
574 Kawakami T (2001a) Tourmaline breakdown in the migmatite zone of the Ryoke metamorphic belt,
575 SW Japan. Journal of Metamorphic Geology 19: 61-75
576 Kawakami T (2001b) Boron depletion controlled by the breakdown of tourmaline in the migmatite

577 zone of the Aoyama area, Ryoke metamorphic belt, SW Japan. Canadian Mineralogist 39:
578 1529-1546
579 Kawakami T (2002) Magmatic andalusite from the migmatite zone of the Aoyama area, Ryoke
580 metamorphic belt, SW Japan, and its importance in constructing the P-T path. Journal of
581 Mineralogical and Petrological Sciences 97: 241-253
582 Kawakami T (2004) Tourmaline and boron as indicators of the presence, segregation and extraction
583 of melt in pelitic migmatites: examples from the Ryoke metamorphic belt, SW Japan.
584 Transactions of the Royal Society of Edinburgh: Earth Sciences 95: 111-124
585 Kawakami T, Ikeda T (2003) Depletion of whole-rock boron controlled by the breakdown of
586 tourmaline and retrograde formation of borosilicates in the Yanai area, Ryoke metamorphic belt,
587 SW Japan. Contributions to Mineralogy and Petrology 145: 131-150
588 Kawakami T, Kobayashi T (2006) Trace element composition and the degree of partial melting of
589 pelitic migmatites from the Aoyama area, Ryoke metamorphic belt, SW Japan: Implications for
590 the source region of tourmaline leucogranites. Gondwana Research 9: 176-188
591 Kawakami T, Nishioka Y (2012) Metamorphic rocks and granitoids in the Aoyama area, Ryoke belt,
592 SW Japan. Journal of the Geological Society of Japan 118 Supplement: 79-89 (in Japanese)
593 Kawakami T, Suzuki K (2011) CHIME monazite dating as a tool to detect polymetamorphism in
594 high-temperature metamorphic terrane – an example from the Aoyama area, Ryoke metamorphic
595 belt, SW Japan. Island Arc 20: 439-453
596 Kretz R (1983) Symbols for rock-forming minerals. American Mineralogist 68: 277-279
597 Ludwig KR (2008) User's manual for Isoplot 3.6. A geological toolkit for Microsoft Excel. Berkeley
598 Geochronology Center Special Publication No.4, revision of April 8, 2008. 77p.
599 Mahar EM, Baker JM, Powell R, Holland TJB, Howell N (1997) The effect of Mn on mineral
600 stability in metapelites. Journal of Metamorphic Geology 15: 223-238
601 Miyashiro A (1965) Metamorphic Rocks and Metamorphic Belts. Iwanami Shoten Publishers, Tokyo.
602 458p. (in Japanese)
603 Morishita R (1992) Crystal size distribution of Togawa andesite lava. Bulletin of Volcanological
604 Society of Japan 37: 285-293 (in Japanese with English abstract)
605 Nakajima T (1994) The Ryoke plutonometamorphic belt: Crustal section of the Cretaceous Eurasian
606 continental margin. Lithos 33: 51-66
607 Okudaira T (1996) Temperature-time path for the low-pressure Ryoke metamorphism, Japan, based
608 on chemical zoning in garnet. Journal of Metamorphic Geology 14: 427-440
609 Okudaira T, Hara I, Sakurai Y, Hayasaka Y (1993) Tectono-metamorphic processes of the Ryoke belt
610 in the Iwakuni-Yanai district, southwest Japan. Memoirs of the Geological Society of Japan 42:
611 91-120
612 Ozaki M, Sangawa A, Miyazaki K, Nishioka Y, Miyachi Y, Takeuchi K, Tagutschi Y (2000) Geology

of the Nara District. With Geological Sheet Map at 1 : 50,000, Geological Survey of Japan, 162p. (in Japanese with English abstract 5p.)

Rubatto D, Hermann J (2007) Zircon behavior in deeply subducted rocks. Elements 3: 31-35

Rubatto D, Williams IS, Buick IS (2001) Zircon and monazite response to prograde metamorphism in the Reynolds Range, central Australia. Contributions to Mineralogy and Petrology 140: 458-468

Schaltegger U, Fanning CM, Gunter D, Maurin JC, Schlmann K, Gebauer D (1999) Growth, annealing and recrystallization of zircon and preservation of monazite in high-grade metamorphism: conventional and in-situ U-Pb isotope, cathodoluminescence and microchemical evidence. Contributions to Mineralogy and Petrology 134: 186-201

Schiøtte L, Compston W, Bridgwater D (1989) Ion probe U-Th-Pb zircon dating of polymetamorphic orthogneisses from northern Labrador, Canada. Canadian Journal of Earth Sciences 26: 1533-1556

Stacey JS, Kramers JD (1975) Approximation of terrestrial lead isotope evolution by a two-stage model. Earth and Planetary Science Letters 26: 207-221

Suzuki K, Adachi M (1998) Denudation history of the high T/P Ryoke metamorphic belt, southwest Japan: constraints from CHIME monazite ages of gneisses and granitoids. Journal of Metamorphic Geology 16: 23- 37

Suzuki K, Adachi M, Kajizuka I (1994) Electron microprobe observations of Pb diffusion in metamorphosed detrital monazites. Earth and Planetary Science Letters 128: 391-405

Tainosho Y, Kagami H, Yuhara M, Nakano S, Sawada K, Morioka K (1999) Highinitial Sr isotopic ratios of Cretaceous to Early Paleogene granitic rocks in Kinki district, Southwest Japan. The memoirs of the Geological Society of Japan 53: 309-321

Takahashi Y, Nishioka Y (1994) Mode of plagioclase twinnings in Ryoke metamorphic rocks in the western area of Tsu City, Mie Prefecture. Journal of the Japanese Association of Mineralogist, Petrologists and Economic Geologists 89: 261-268 (in Japanese with English abstract)

Thomas JB, Bodnar RJ, Shimizu N, Chesner CA (2003) Melt inclusions in zircon. Reviews in Mineralogy and Geochemistry 53: 63-87

Tunheng A, Hirata T (2004) Development of signal smoothing device for precise elemental analysis using laser ablation-ICP-mass spectorometry. Journal of Analytical Atomic Spectrometry 19: 932-934

Vavra G, Gebauer D, Schmid R, Compston W (1996) Multiple zircon growth and recrystallization during polyphase Late Carboniferous to Triassic metamorphism in granulites of the Iverea Zone (Southern Alps): an ion microprobe (SHRIMP) study. Contributions to Mineralogy and Petrology 122: 337-358

Vavra G, Schmid R, Gebauer D (1999) Internal morphology, habit and U-Th-Pb microanalysis of

amphibolite-to-granulite facies zircons: geochronology of the Iverea Zone (Southern Alps). Contributions to Mineralogy and Petrology 134: 380-404

Wakita K (1987) The occurrence of Latest Jurassic - Earliest Cretaceous radiolarians at the Hida-Kanayama area in the Mino terrane, central Japan. The Journal of Geological Society of Japan 93: 441-443

Wei CJ, Powell R, Clarke GL (2004) Calculated phase equilibria for low- and medium-pressure metapelites in the KFMASH and KMnFMASH systems. Journal of Metamorphic Geology 22: 495-508

Wiedenbeck M, Alle P, Corfu F, Griffin WL, Meier M, Oberli F, Von Quadt A, Roddick JC, Spiegel W (1995) Three natural zircon standards for U-Th-Pb, Lu-Hf, trace element and REE analyses. Geostandards Newsletter 19: 1-23

Wiedenbeck M, Hanchar JM, Peck WH, Sylvester P, Valley J, Whitehouse M, Kronz A, Morishita Y, Nasdala L, Fiebig J, Franchi I, Girard J–P, Greenwood RC, Hinton R, Kita N, Mason PRD, Norman M, Ogasawara M, Piccoli PM, Rhede D, Satoh H, Schulz-Dobrick D, Skår Ø, Spicuzza MJ, Terada K, Tindle A, Togashi S, Vennemann T, Xie Q, Zheng Y–F (2004) Further characterisation of the 91500 zircon crystal. Geostandards and Geoanalytical Research 28: 9-39.

Yoshida F, Takahashi Y, Nishioka Y (1995) Geology of the Tsu-Seibu district. With geological sheet map at 1:50,000. Geological Survey of Japan. (in Japanese with English abstract)

Yoshizawa H, Nakajima W, Ishizaka K (1966) The Ryoke metamorphic zone of the Kinki district, Southwest Japan: Accomplishment of a regional geological map. Memoirs of the College of Science, University of Kyoto, Series B 32: 437-453

**Figure captions**

Fig. 1 (a) Simplified geological map of the Ryoke metamorphic belt. The low-temperature, high-pressure type Sanbagawa belt is located to the south of the Ryoke metamorphic belt and these two belts are separated by the Median Tectonic Line (MTL). (b) Geological map of the Aoyama area (after Yoshida et al. 1995; Ozaki et al. 2000) showing the sample localities. The Grt-Crd and tourmaline-out isograds (Kawakami 2001a) are subparallel to the schist/migmatite boundary and to the penetrative schistosity and migmatitic banding observed in this area. Sample names shown next to locality points correspond to those given in Table 1.

Fig. 2. A diagram showing the whole-rock Zr concentration versus modal amount of zircon (> 20 μm). Density of the rock and zircon were assumed to be 2.7 g/cm$^3$ and 4.6 g/cm$^3$, respectively. Each diamond and square pair connected by a solid line represent a dataset from a single sample, based on the different assumption made in calculating the modal amount of zircon in a single

thin section as follows: (i) assuming ellipsoidal shape of zircon, plotted as low-modal amount points, and (ii) assuming rectangular shape of zircon, plotted as high-modal amount points. Broken lines and numbers (%) shown in the figure represents the percentage of whole-rock Zr content hosted by the zircon (> 20 μm).

Fig. 3 A plot showing the result of grain size distribution of zircon in a metatexite sample AN44, determined by the X-ray elemental mapping of the whole thin section (open diamonds). Numerical expression given in the figure is that for the least squares fit of the solid triangle data (solid line). A broken line represents the least squares fit for the gray square points. See text for further explanation.

Fig. 4. A summary of the CSD plots for 2 schist samples (Fig. 4a, b), 4 metatexite samples (Fig. 4c-f), and 4 diatexite samples (Fig. 4g-k). All the zircon grain size (major axis) data were measured by BSE image observation utilizing WDS. Sample numbers are given in the top right of each figure (AN32 etc.). See Fig. 1b for the sample locality and Table 1 for sample descriptions. (j) is an enlargement of the fine-grained portion of (i). See text for details.

Fig. 5. The BSE and CL images of zircon in diatexites from the Grt-Crd zone of the Aoyama area. Red circles represent the size of pits created by LA-ICP-MS U-Pb dating and numbers given are the $^{206}Pb/^{238}U$ age ± 2SD error [better than 95-105% concordance except for the points at young rim of (b) 93%, (f) 93%, and (l) 94%, where concordance = ($^{206}Pb/^{238}U$ age)*100/($^{207}Pb/^{235}U$ age)] and Th/U ratio. These relatively low concordance data points are shown so that correlation with zircon microstructure is clear. '*' represents that the point gave discordant data. Scale bars are 10 μm. Red arrows indicate the melt (presently glass) and mineral (biotite, quartz, plagioclase and K-feldspar) inclusions included along the thin, bright annulus under BSE image. This annulus is recognized as dark annulus in CL image. Red dotted line represents the core/rim boundary where dark-CL annulus is truncated by the brighter-CL overgrowth. (a), (c), (e), (g), (i) and (k); CL image of zircon grains from a diatexite (G6-28, G6-31, G6-4, G6-34, G6-38, and G6-17, respectively). (a), (c), (e) and (i) are in the matrix, and (g) and (k) are included in biotite. (b), (d), (f), (h), (j) and (l); BSE images of (a), (c), (e), (g), (i) and (k), respectively. (m) CL image of a newly nucleated zircon grain at 86.7 ± 9.2 Ma present in the matrix of diatexite (Y32-38). Note the similar CL-brightness as the outermost part of the rim overgrowth shown in (a), (c), (e), (g), (i) and (k). (n) BSE image of (m). (o), (q), (s), (u) and (w) CL images of zircon grains from a garnet-bearing diatexite (G11-19, G11-13, G11-16, G11-21 and G11-18, respectively). (q) occurs as an inclusion in garnet, and others are found in the matrix. (w) has tiny inclusion alignment along a dark-CL annulus under transmitted light microscope, but not

exposed on the surface. (p), (r), (t), (v) and (x); BSE images of (o), (q), (s), (u) and (w).

Fig. 6. Bright and dark field images of TEM sample as a whole (sample G6), enlargement of inclusions in it (inclusions 1-5) and electron diffraction patterns of the inclusions. Width of the sample is 9.2 μm. Host mineral of the inclusions is zircon. Diffuse halo pattern clearly shows that inclusions are the glass (inclusions 1, 3 and 5), or the mixture of the glass and crystal (inclusions 2 and 4). Most of the spotted electron diffraction patterns are from host zircon except for inclusions 2 and 4. Red arrows shown in the photo of inclusion 2 are 'nano-porosities' after Cesare et al. (2011). The EDS analysis under TEM shows that inclusion 3 is a glass containing K, Al and Si, and inclusion 1 is a Si-rich glass.

Fig. 7. (a) Concordia diagram for the LA-ICP-MS U-Pb dating of zircon from the diatexite-dominant part of the Grt-Crd zone. Concordia diagrams in this study are constructed using Isoplot 3.6 (Ludwig 2008). Since the thickness of rim and the size of the newly-nucleated zircon sometimes reach more than 20 μm in the diatexite-dominant part of the Grt-Crd zone, LA-ICP-MS dating of the rim can be done without any mixing of the core. However, some of the analyses are the mixed analysis of the core and the rim, resulting in the discordia-like mixing line. Inset is an enlargement of the young-aged part. (b) Concordia diagram for selected analyses of zircon rim and newly-nucleated zircon grain. The result of concordia age calculation is also shown.

Fig. 8. The BSE and CL images of zircon in a psammitic schist AN16 and a pelitic schist AN24 from the Grt-Crd zone. Red circles represent the size of pits created by LA-ICP-MS U-Pb dating and numbers given are the $^{206}Pb/^{238}U$ age ± 2SD error. (a), (c), (e), (g), (i), (k), (m), (o), (q), (s) and (u); BSE images of zircon. (a) AN16-re13 in matrix, (c) AN16-11 in matrix, (e) AN16-13 in matrix, (g) AN16-07 in matrix, (i) AN16-24 in matrix, (k) AN16-re35 in matrix, (m) AN16-22 in matrix, (o) AN16-29 in matrix, (q) AN24-31 in matrix, (s) AN24-re02 in quartz, and (u) AN24-re15 in plagioclase, respectively. (b), (d), (f), (h), (j), (l), (n), (p), (r), (t) and (v); CL images of (a), (c), (e), (g), (i), (k), (m), (o), (q), (s) and (u).

Fig. 9. The BSE and CL images of zircon in metatexites from the Grt-Crd zone. Red arrows indicate the melt and mineral inclusions included along the thin, bright annulus under BSE image (identical with the dark-CL annulus). Red circles represent the size of pits created by LA-ICP-MS U-Pb dating and numbers given are the $^{206}Pb/^{238}U$ age ± 2SD error. (a), (c), (e), (g), (i), (k), (m), (o), (q) and (s); CL images of zircon from metatexite samples AN07a, AN27 and AN52. (a) AN07a-1 in garnet, (c) AN07a-3 in retrograde muscovite, (e) AN07-17 in matrix, (g) AN52-25 in matrix, (i) AN07a-2 in garnet, (k) AN07a-12 in matrix, (m) AN07a-07 in biotite, (o)

AN52-06 in matrix, (q) AN07-21 in matrix, and (s) AN27-06 in matrix, respectively. (b), (d), (f), (h), (j), (l), (n), (p), (r) and (t); BSE images of (a), (c), (e), (g), (i), (k), (m), (o), (q) and (s).

Fig. 10. Concordia diagram for the LA-ICP-MS U-Pb dating of zircon from the schist-dominant and metatexite-dominant parts of the Grt-Crd zone. Since the development of the zircon rim is not sufficient enough for LA-ICP-MS dating with 20 μm spot size, mixed analysis was intentionally performed on rims, resulting in the discordia (mixing line) on the diagram. Inset is an enlargement of the young-aged part.

Fig. 11. A *P-T-t* path for the low-temperature part of the Grt-Crd zone (schist-migmatite boundary) of the Aoyama area. Modified after Kawakami (2002). Pseudosection shown in the suprasolidus *P-T* region is from Wei et al. (2004) constructed for KMnFMASH + quartz system using typical pelite composition ($M_{Mn}$ = Mn/(Mn+Fe+Mg) = 0.007) of Mahar et al. (1997). Their calculation shows that increase of $M_{Mn}$ widens the stability field of garnet + cordierite assemblage very much. With $M_{Mn}$ = 0.03, garnet + cordierite is stable in subsolidus field even at 2 kbar, 650 $^{o}$C (not shown). This is consistent with the whole-rock Mn content of pelitic metamorphic rocks in the Aoyama area (Kawakami 2001b; Kawakami and Kobayashi 2006) and with the field observation that garnet + cordierite assemblage is found not only in migmatite-dominant area but also in the schist-dominant area. Therefore, effect of Mn is responsible for the low-temperature estimates obtained for the Grt-Crd zone samples. Timing of the monazite growth is considered to be the prograde stage (first attainment of 525 $^{o}$C, pressure not constrained; Suzuki and Adachi 1998), and the zircon rim growth to be near-peak metamorphic condition to the retrograde, melt crystallization stage. Zircon rim growth stage is shown by a thick gray arrow.

Table 1. Summary of the description of samples and the result of whole-rock trace element analyses. Trace element data were obtained for thin-section sized chips by XRF. Crd(?) in the mineral assemblage of sample AN24 represents that alteration that looks like a pseudomorph after Crd is present.

Table 2. Instrumental settings of the LA-ICP-MS U-Pb zircon dating at Department of Geology and Mineralogy, Kyoto University.

Table 3. Representative results of the LA-ICP-MS U-Pb zircon dating that were used for the calculation of 90.3 ± 2.2 Ma concordia age. Most of the $^{204}$Pb listed in the table are actually $^{204}$Hg as calculated from $^{202}$Hg counts. No common Pb correction was applied.

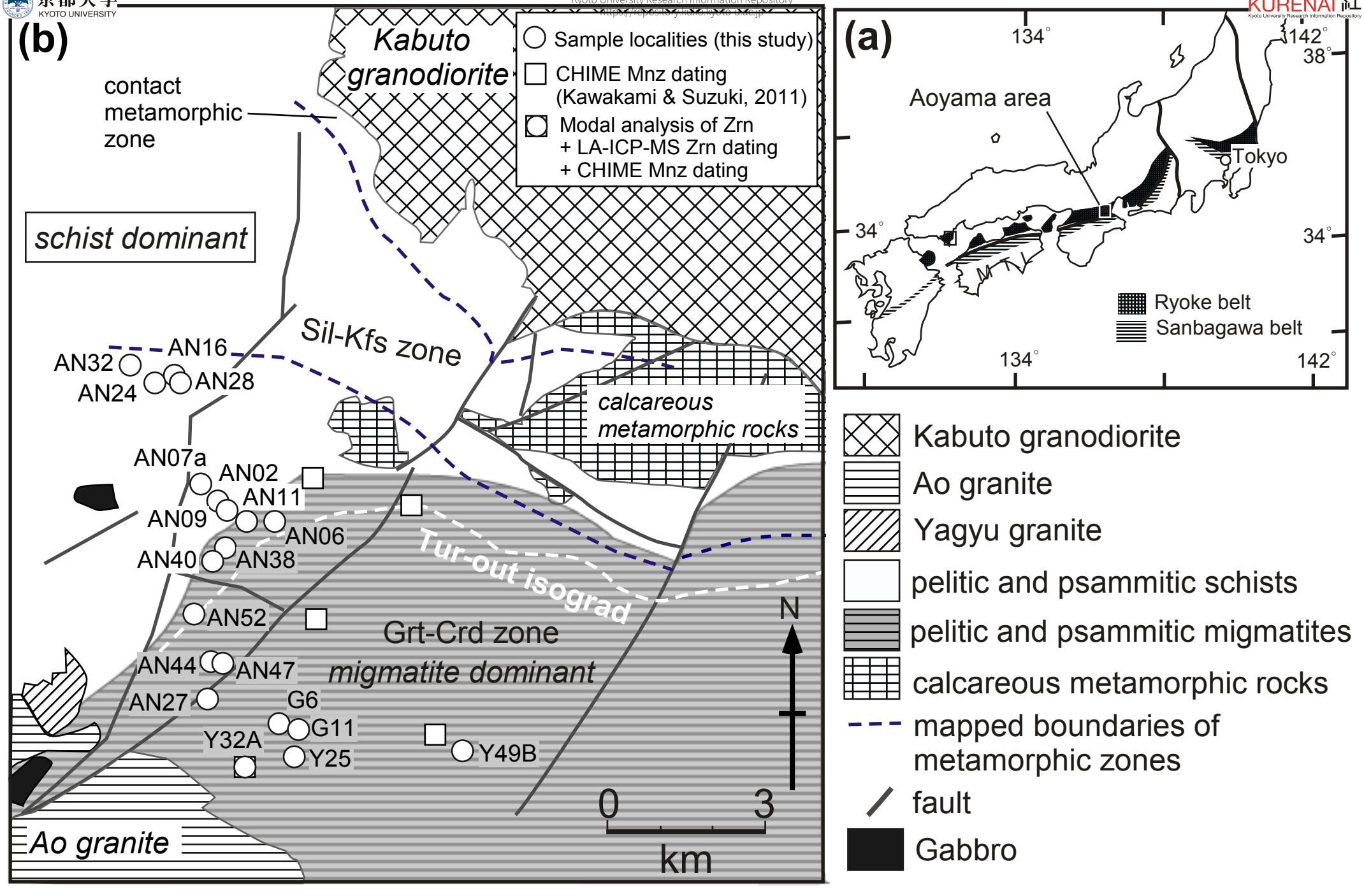


Kawakami et al. Fig. 1

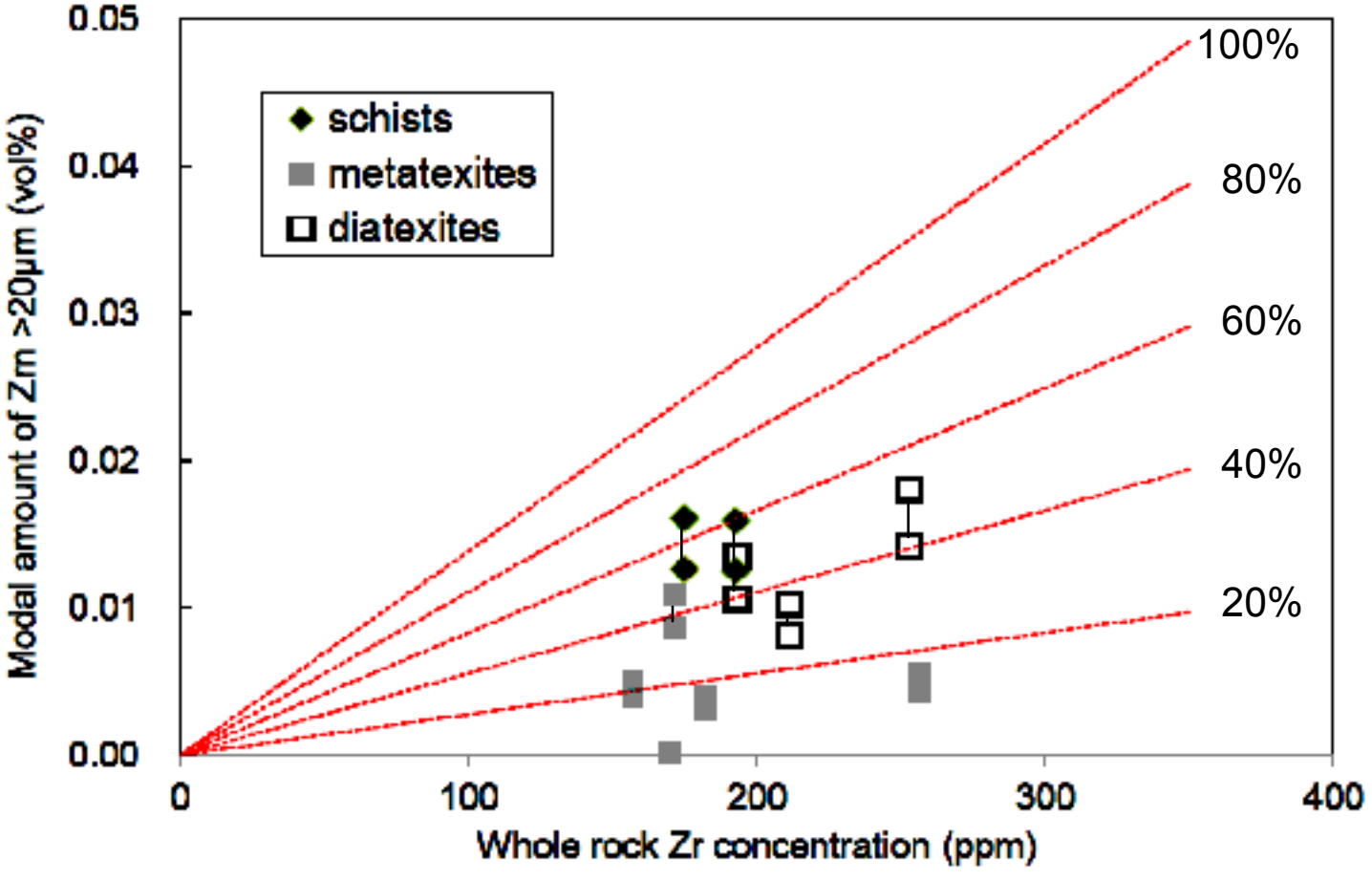


Kawakami et al. Fig. 2

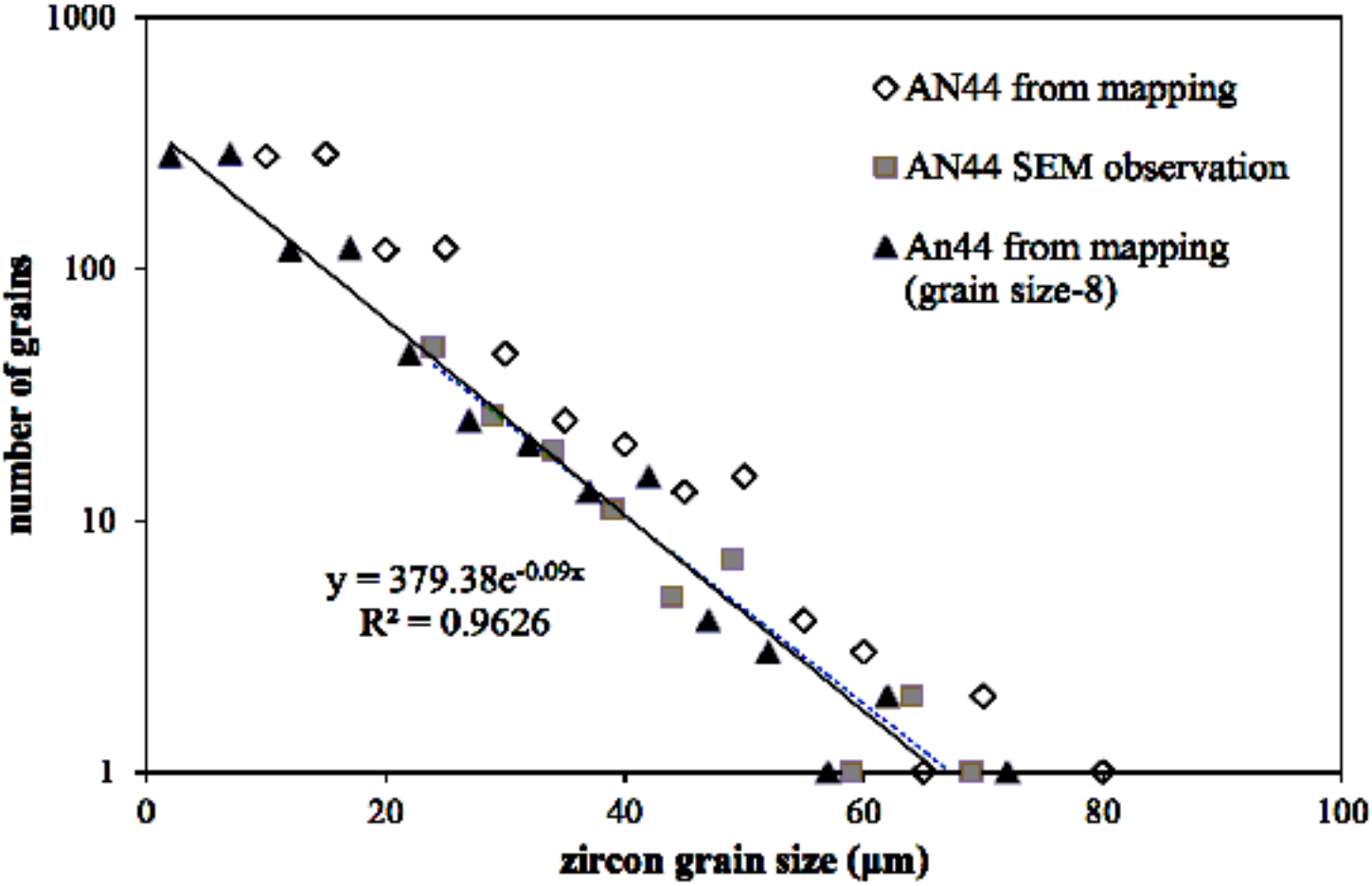


Figure 3 Kawakami et al.

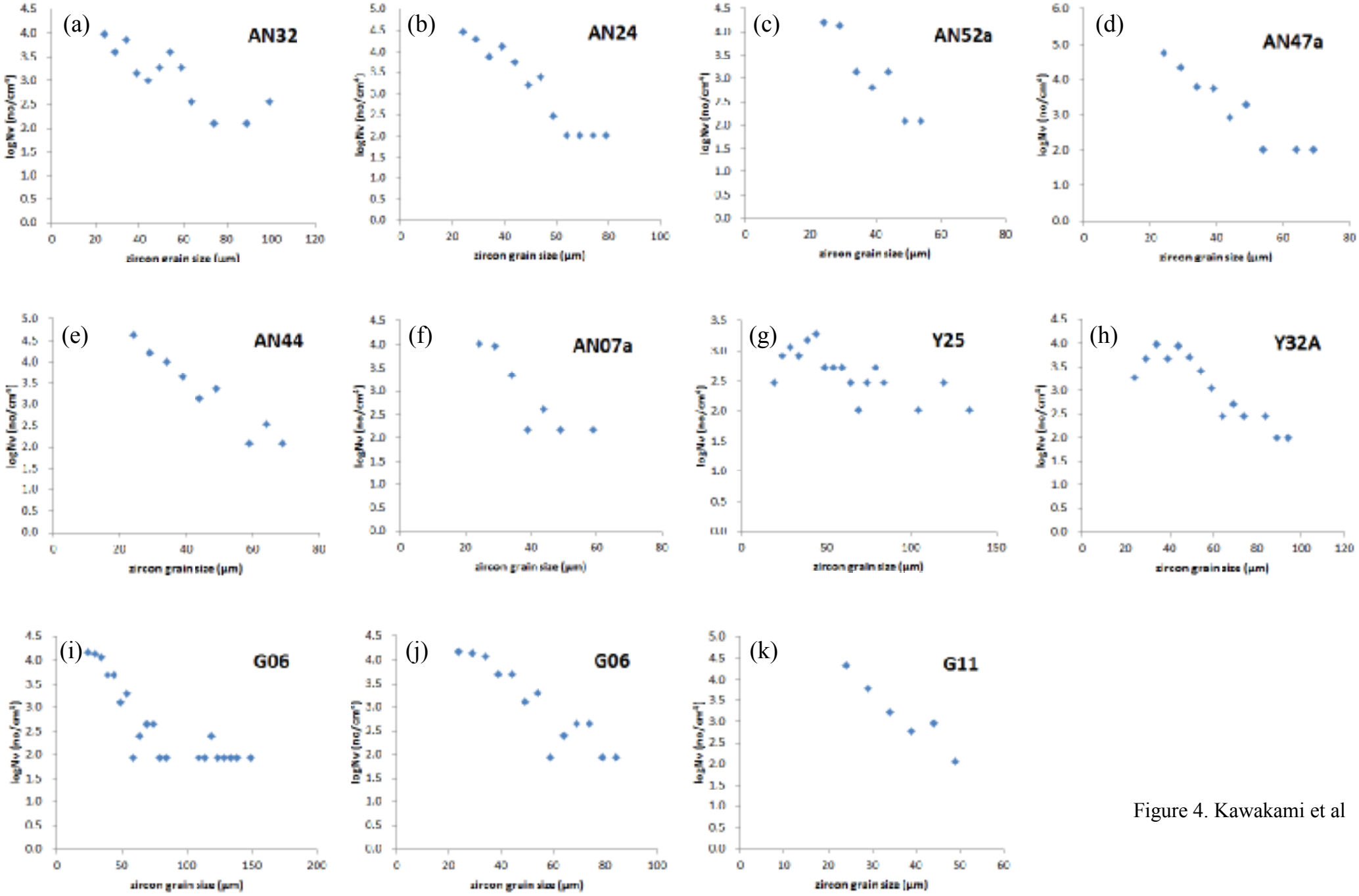


Figure 4. Kawakami et al

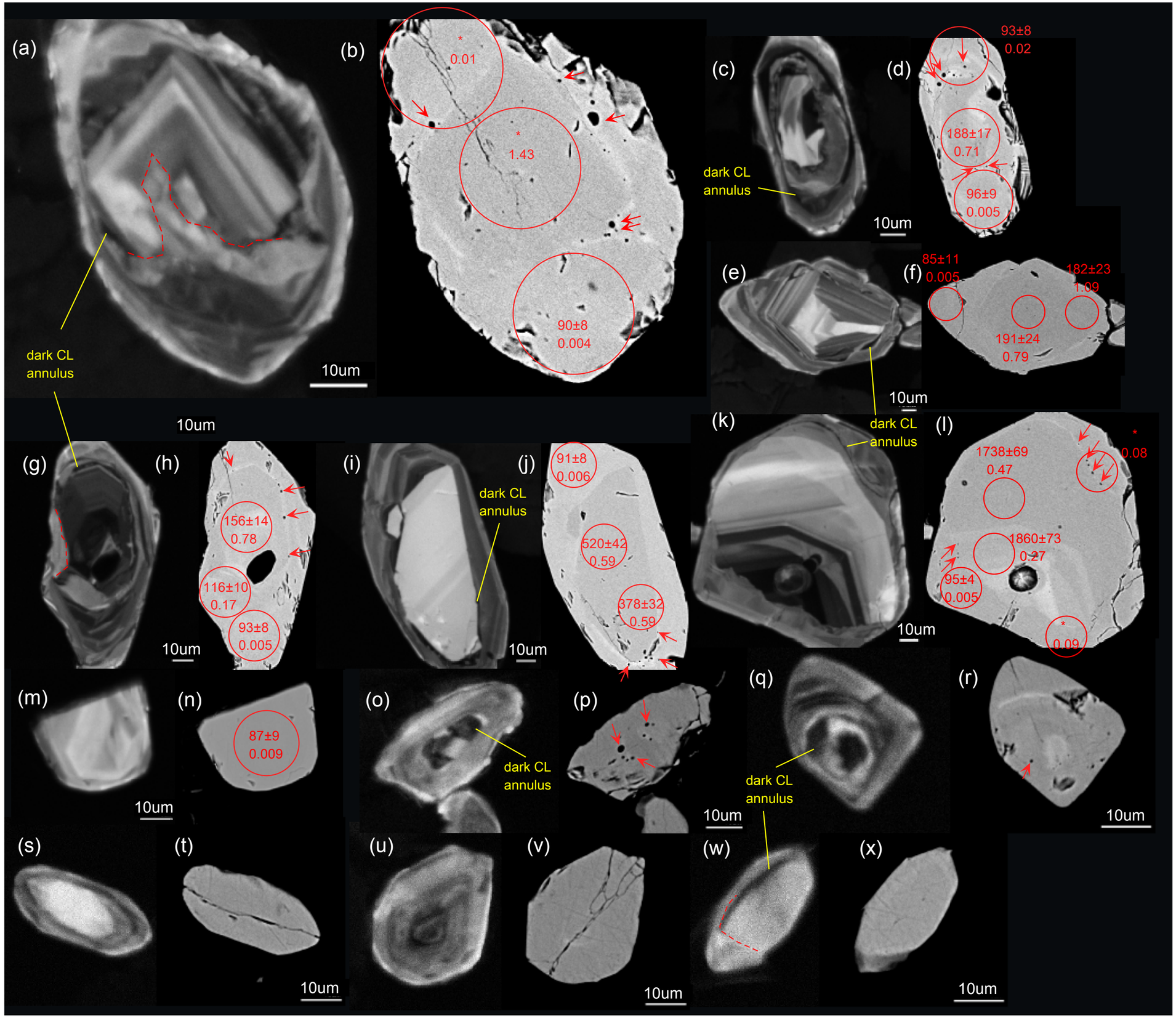


Kawakami et al Fig. 5 (full page width)

# *Sample G6*

## inclusion 2: Kfs + glass

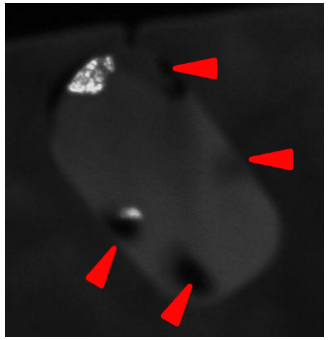

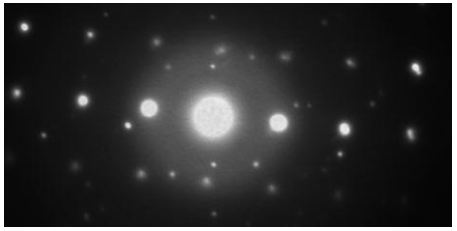

## inclusion 1: glass (Si-rich)

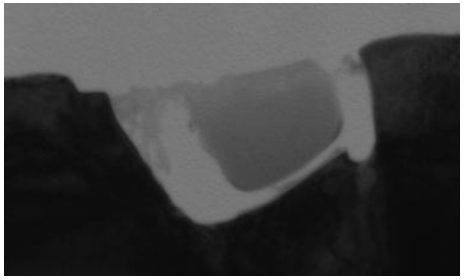

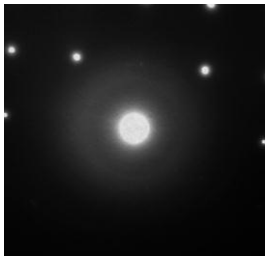

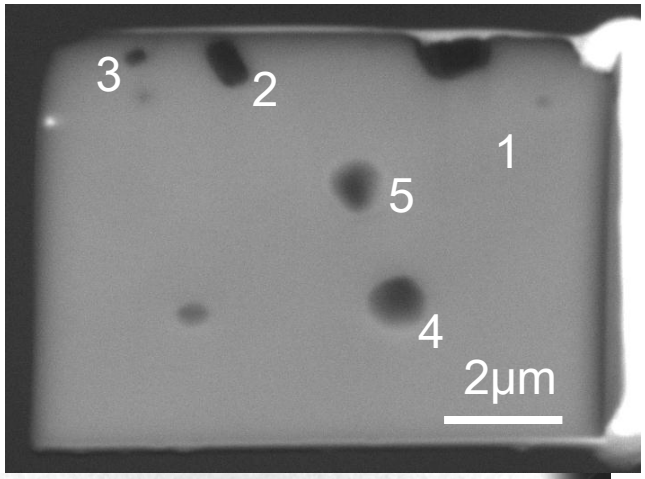


## inclusion 3: glass (K,Al,Si-rich)

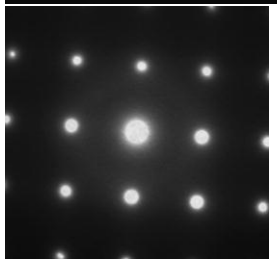

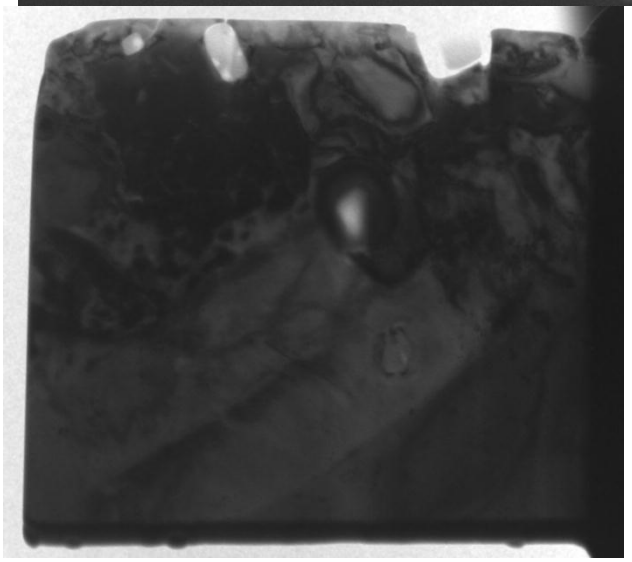

## inclusion 5: glass

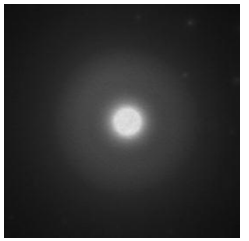

## inclusion 4: crystal

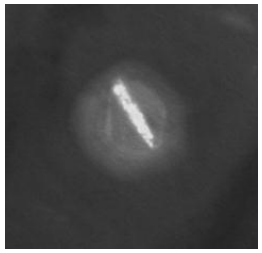

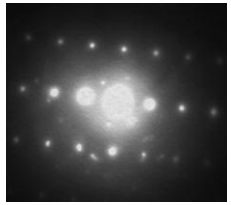

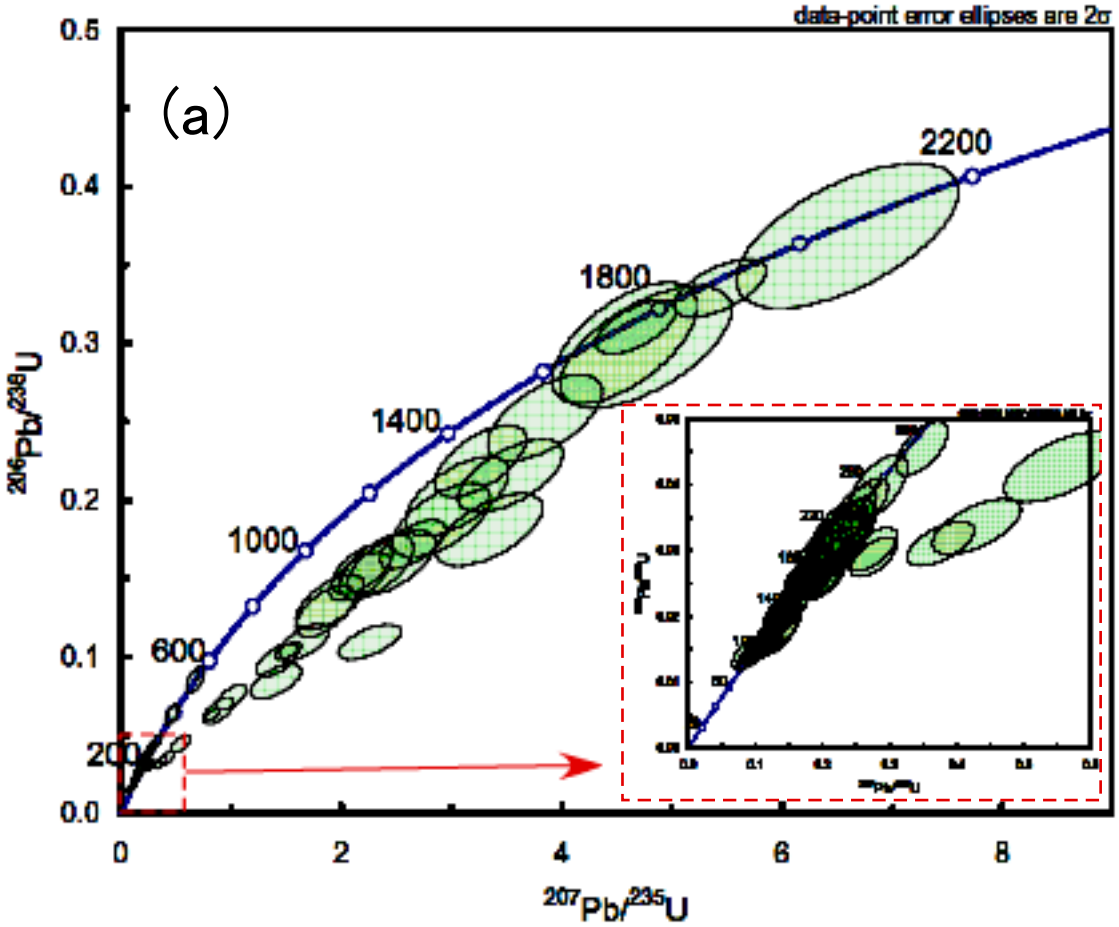


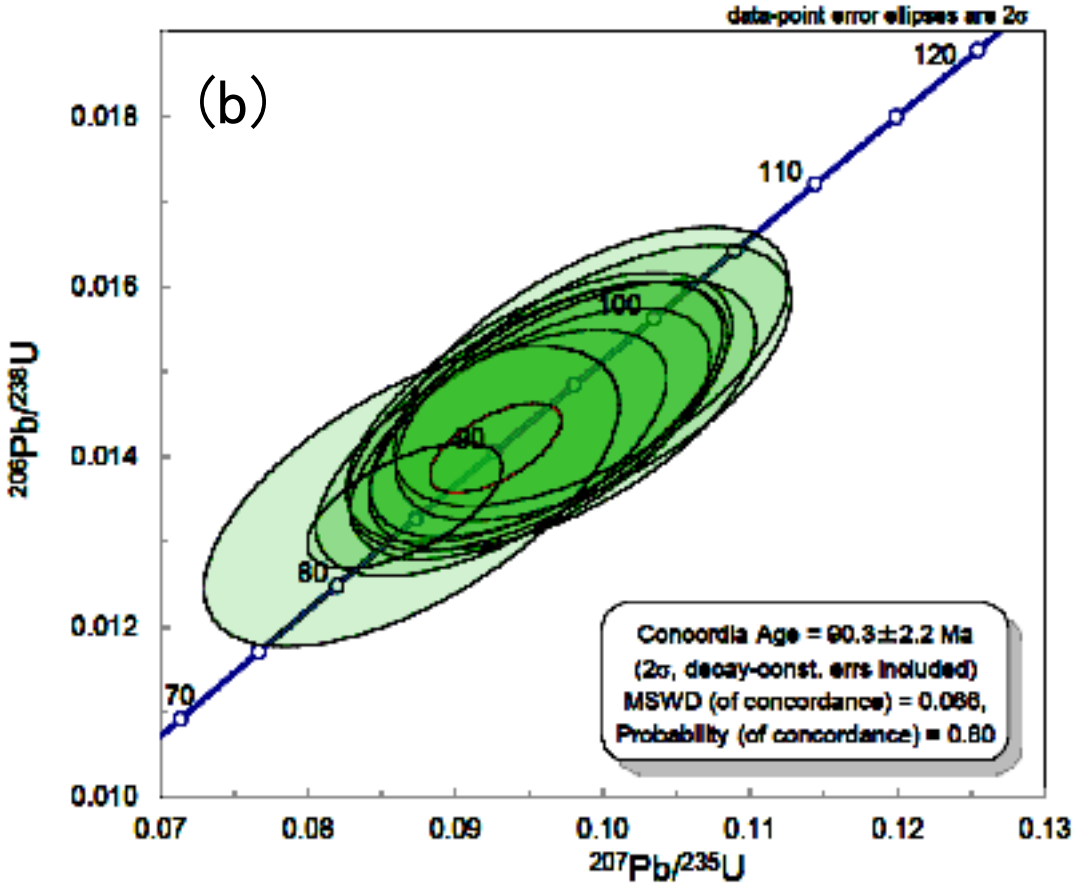


Figure 7 Kawakami et al.

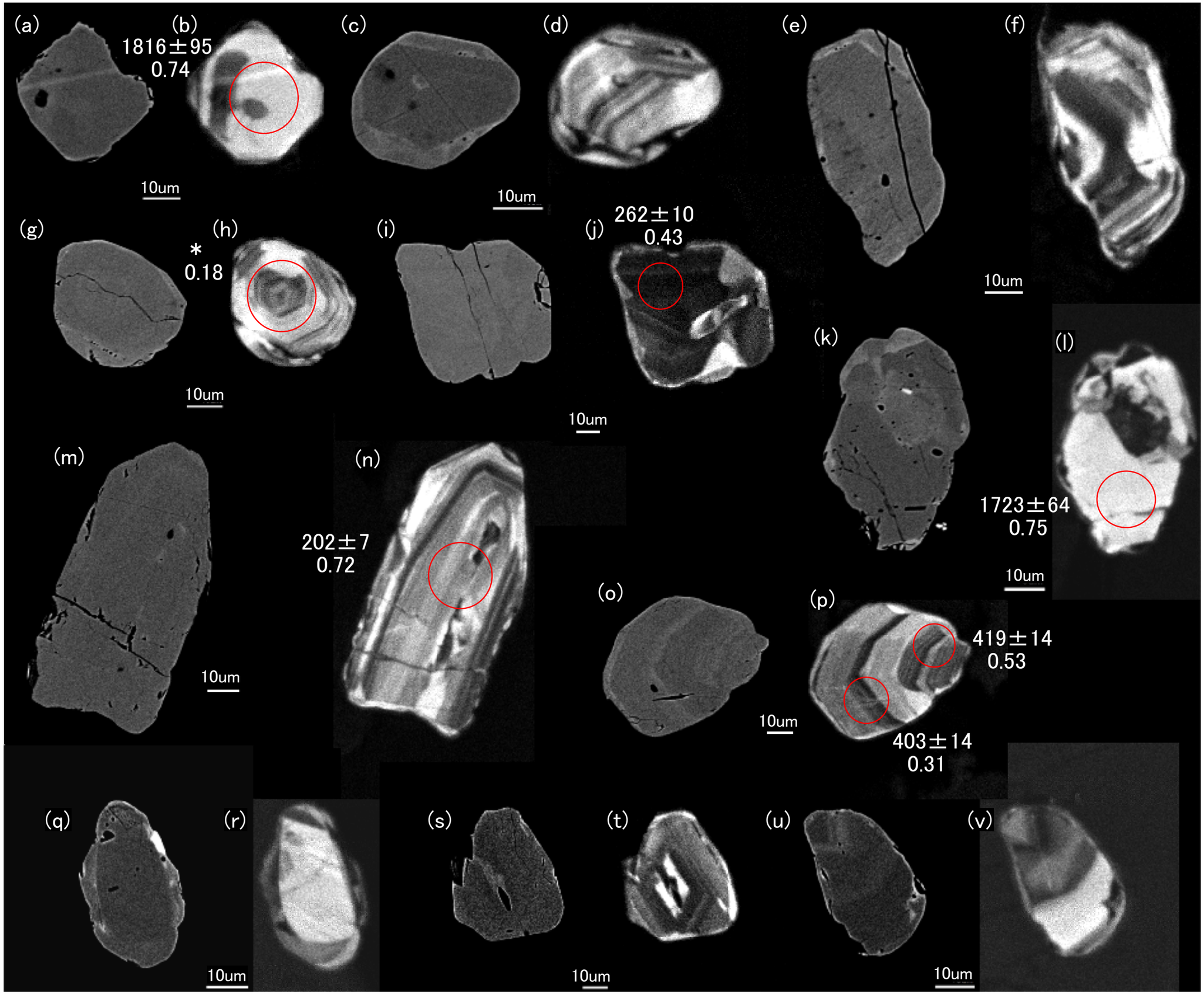


Kawakami et al Fig. 8

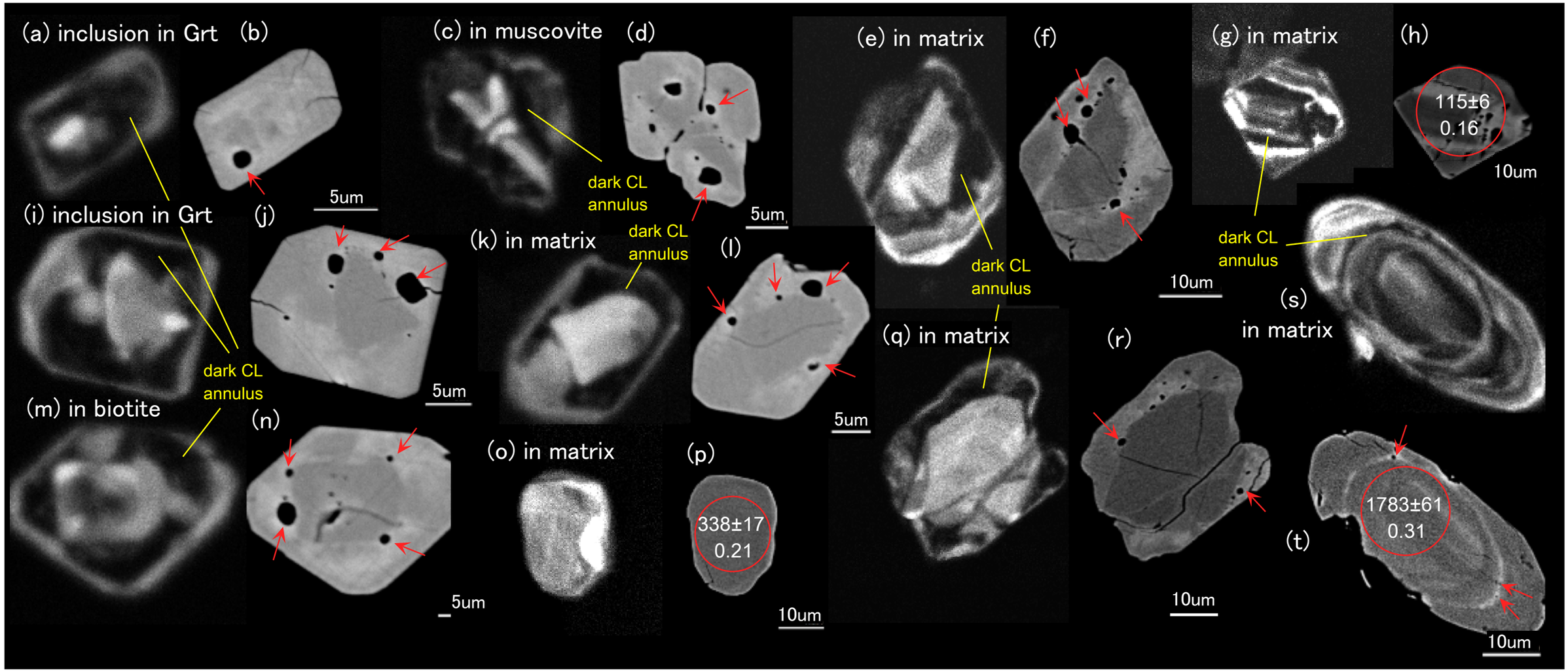


Kawakami et al. Fig. 9

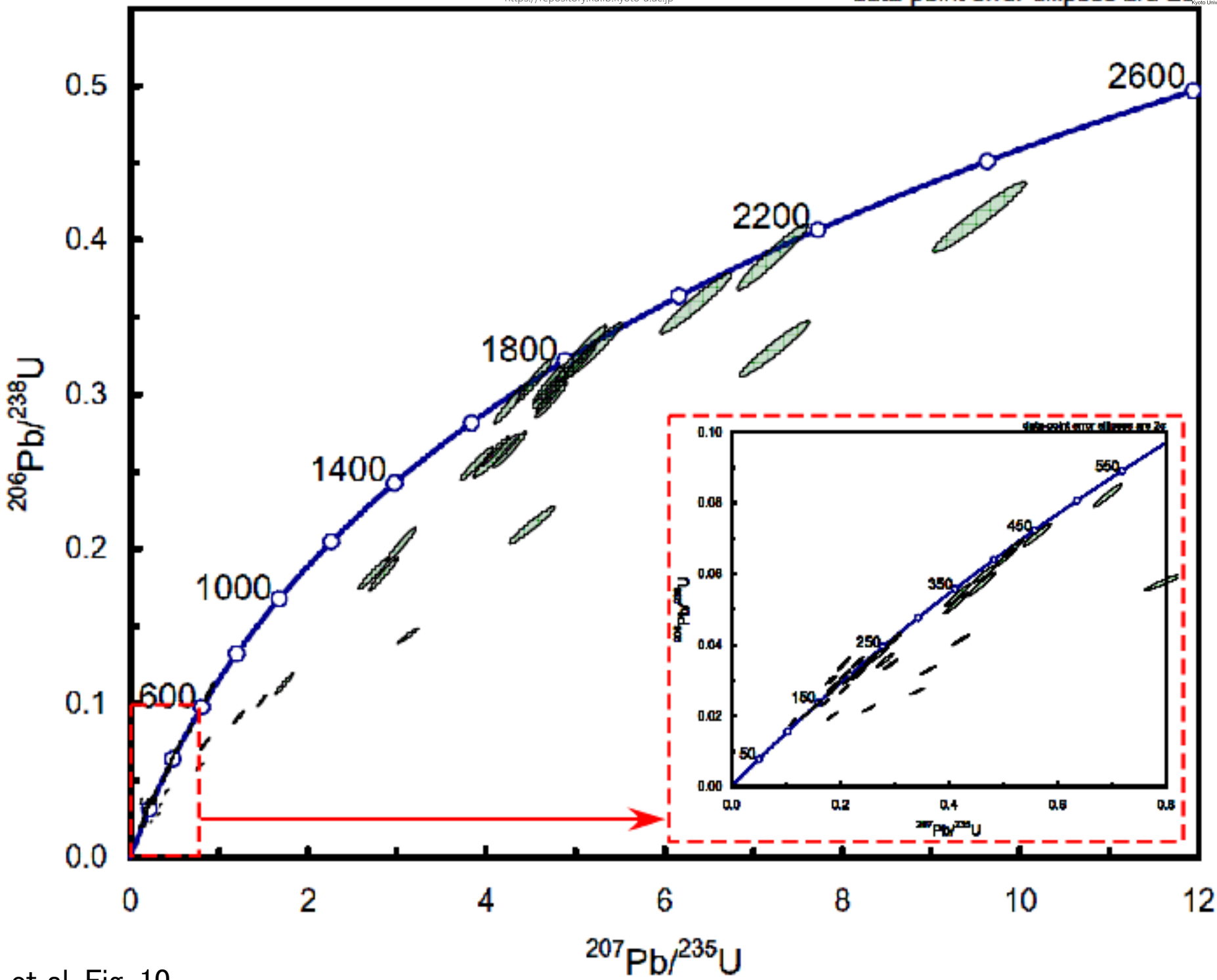


Kawakami et al. Fig. 10

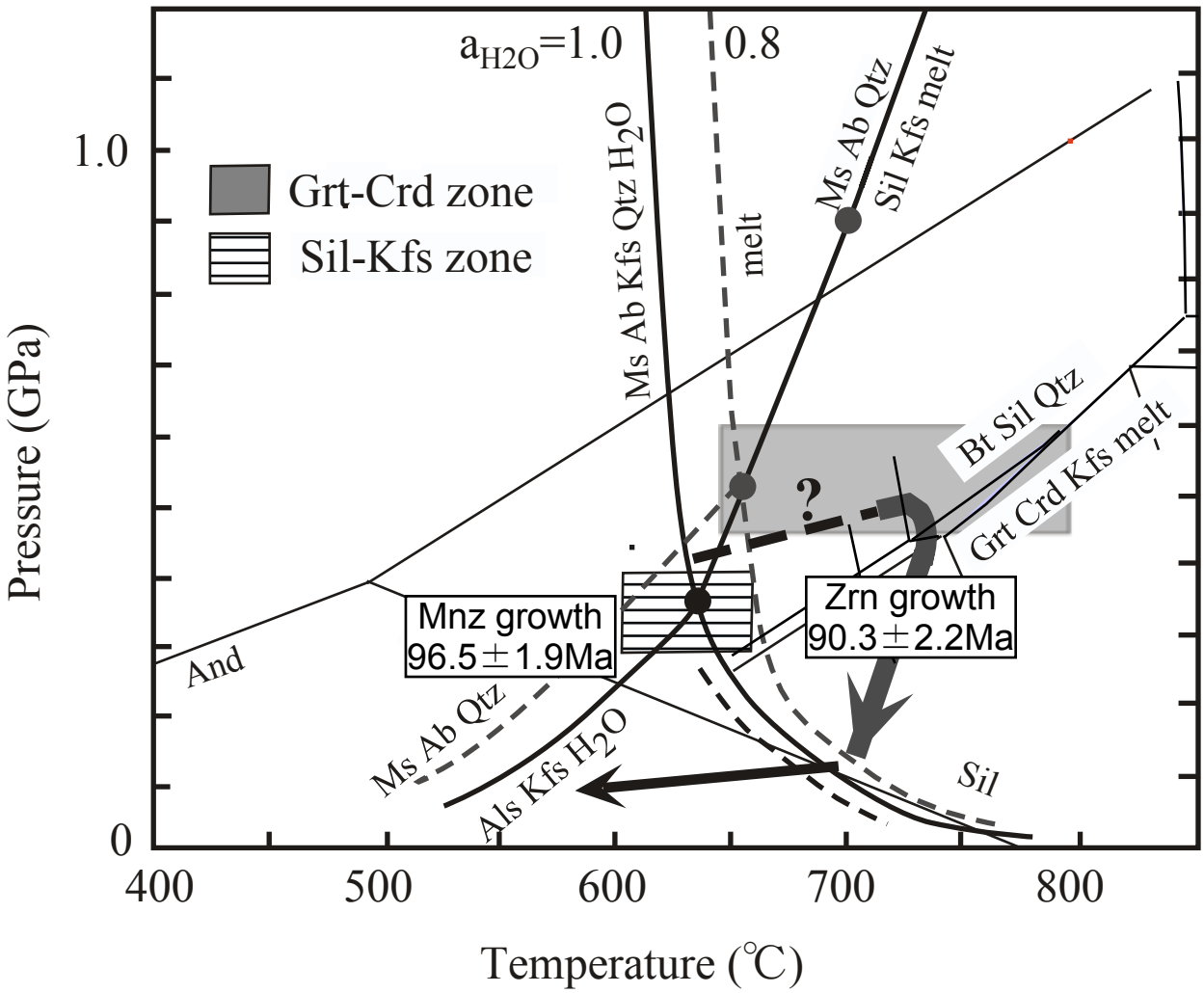


Fig. 11 Kawakami et al.

| sample | location in the Grt-Crd zone | rock type | dark-CL annulus with inclusions | mineral assemblage (+Pl+Kfs+Qtz± retrograde Ms) | LA-ICP-MS Zrn dating | modal amount of Zrn>20μm (vol%) | modal amount of Zrn>20μm (vol%) rectangle | trace element concentration (ppm) | | | | | | | | |
|---|---|---|---|---|---|---|---|---|---|---|---|---|---|---|---|---|
| | | | | | | | | Cr | Ni | Ba | Rb | Nb | Pb | Sr | Zr | Y |
| AN16 | north | psammitic schist | scarce | Bt | ○ | – | – | 33 | 24 | 1266 | 104 | 8 | 27 | 234 | 313 | 20 |
| AN24 | north | pelitic schist | scarce | Bt+Crd(?) | ○ | 0.013 | 0.016 | 49 | 24 | 1312 | 111 | 10 | 25 | 257 | 193 | 21 |
| AN32 | north | psammitic schist | scarce | Bt | ○ | 0.013 | 0.016 | 29 | 21 | 384 | 91 | 6 | 18 | 214 | 119 | 11 |
| AN28 | middle | metatexite | common | Bt+Grt+Crd | – | – | – | 45 | 29 | 510 | 64 | 9 | 9 | 108 | 105 | 15 |
| AN02 | middle | metatexite | common | Bt+Grt+Sil+Tur | – | 0.0002 | 0.0002 | 48 | 47 | 677 | 128 | 9 | 31 | 112 | 170 | 29 |
| AN06 | middle | metatexite | common | Bt+Crd+Tur | – | – | – | 56 | 48 | 962 | 192 | 10 | 30 | 281 | 249 | 25 |
| AN07a | middle | metatexite | common | Bt+Grt+Tur | – | 0.003 | 0.003 | 50 | 24 | 505 | 116 | 10 | 28 | 228 | 182 | 28 |
| AN09 | middle | metatexite | scarce | Bt+Grt (+Sil inc) | – | – | – | 46 | 35 | 766 | 112 | 10 | 20 | 113 | 195 | 28 |
| AN11 | middle | metatexite | common | Bt+Grt | – | – | – | 72 | 44 | 179 | 105 | 6 | 16 | 190 | 131 | 27 |
| AN38 | middle | metatexite | common | Bt+Grt+Crd | – | – | – | 34 | 26 | 225 | 84 | 7 | 16 | 145 | 177 | 37 |
| AN40 | middle | metatexite | common | Bt+Grt+Crd+Tur | – | – | – | 125 | 54 | 378 | 101 | 8 | 20 | 226 | 176 | 37 |
| AN47 | middle | metatexite | common | Bt+Grt+Crd (+Sil inc) | ○ | 0.009 | 0.011 | 62 | 28 | 421 | 130 | 8 | 17 | 159 | 172 | 24 |
| AN44 | middle | metatexite | common | Bt+Grt+Crd+Sil | ○ | 0.004 | 0.005 | 66 | 25 | 253 | 108 | 12 | 18 | 129 | 257 | 45 |
| AN52 | middle | metatexite | common | Bt+Grt | ○ | 0.004 | 0.005 | 52 | 30 | 249 | 85 | 9 | 22 | 285 | 157 | 29 |
| AN27 | middle | metatexite | common | Bt+Grt+Crd+Sil | ○ | – | – | 75 | 48 | 860 | 206 | 16 | 27 | 147 | 177 | 31 |
| Y49B | south | metatexite | common | Bt+Grt+Crd+Sil | – | – | – | - | - | - | - | - | - | - | - | - |
| Y32A | south | diatexite | common | Bt+Crd+Sil | ○ | 0.014 | 0.018 | 71 | 29 | 353 | 130 | 17 | 20 | 229 | 253 | 27 |
| Y25 | south | diatexite | common | Bt+Crd+Sil | ○ | 0.011 | 0.013 | 73 | 40 | 589 | 167 | 19 | 23 | 209 | 193 | 22 |
| G6 | south | diatexite | common | Bt | ○ | 0.008 | 0.010 | 109 | 47 | 258 | 96 | 14 | 21 | 232 | 211 | 17 |
| G11 | south | diatexite | rare | Bt+Grt+Sil | – | 0.003 | 0.004 | 34 | 27 | 428 | 103 | 18 | 18 | 128 | 194 | 43 |

Table 1 Kawakami et al.

| | | | |
|---|---|---|---|
| **Nu AttoM single collector ICP-MS** | | | |
| RF power | 1350 W | | |
| Cooling gas flow rate | 13 l /min | | |
| Auxiliary gas flow rate | 0.9 l /min | | |
| Detection system | Mixed attenuation-multiple ion counting | | |
| IC dead time | 18 ns | | |
| | | | |
| **NWR193 excimer laser system** | | | |
| ATLEX-SI ArF excimer laser | | | |
| Wavelength | 193 nm | | |
| Pulse energy | 7.0 mJ | | |
| Pulse width | 4-6 ns | | |
| Energy density/ Fluence | 1.60-2.23 J /cm$^2$ | | |
| Repeatition rate | 6 Hz | | |
| Spot diameter | 20 μm | | |
| Helium carrier gas flow rate | 1.00 l /min | | |
| Argon make-up gas flow rate | 1.05 l /min | | |
| Signal smoothing device | with | | |
| Number of laser shots | 100 shots | | |
| | | | |
| **Measured isotope** | Dwell time | | Attenuation |
| | Sample | Gas blank | |
| $^{202}$Hg | 1300 ms | 2000 ms | Off |
| $^{204}$Pb | 1300 ms | 2000 ms | Off |
| $^{206}$Pb | 1300 ms | 2000 ms | Off |
| $^{207}$Pb | 1300 ms | 2000 ms | Off |
| $^{208}$Pb | 1300 ms | 2000 ms | Off |
| $^{232}$Th | 1300 ms | 2000 ms | Off |
| $^{238}$U | 1300 ms | 2000 ms | On or Off |
| Data acquired time | 11 sec | 150 sec | |

Kawakami et al. Table 2

| 7th July 2011, Department of Geology and Mineralogy, Kyoto University | | | | | | | | | | | | | Ages (Ma) | | | | |
|---|---|---|---|---|---|---|---|---|---|---|---|---|---|---|---|---|---|
| Grain number | $^{204}$Pb (cps) | $^{202}$Hg (cps) | U (ppm) | Th (ppm) | Th/U | $^{204}$Pb/$^{206}$Pb | $^{206}$Pb/$^{238}$U | ±2SD | $^{207}$Pb/$^{235}$U | ±2SD | $^{207}$Pb/$^{206}$Pb | ±2SD | $^{206}$Pb/$^{238}$U age | ± 2SD | $^{207}$Pb/$^{235}$U age | ±2SD abs | U-Pb discordance (%) |
| G6-15 | 1756 | 7487 | 660 | 3.1 | 0.005 | 0.0537 | 0.0134 | 0.0006 | 0.0866 | 0.0054 | 0.0465 | 0.0019 | 86.0 | 3.9 | 84.3 | 5.1 | -2.0 |
| G6-29 | 1783 | 7571 | 747 | 13.0 | 0.017 | 0.0538 | 0.0145 | 0.0013 | 0.0973 | 0.0107 | 0.0485 | 0.0019 | 92.8 | 8.2 | 94.3 | 9.9 | 1.6 |
| G6-30 | 1720 | 7722 | 617 | 5.5 | 0.009 | 0.0538 | 0.0149 | 0.0013 | 0.0994 | 0.0110 | 0.0483 | 0.0019 | 95.2 | 8.4 | 96.2 | 10.1 | 1.1 |
| G6-31 | 1785 | 7514 | 934 | 4.1 | 0.004 | 0.0538 | 0.0151 | 0.0013 | 0.0993 | 0.0109 | 0.0476 | 0.002 | 96.4 | 8.5 | 96.1 | 10.1 | -0.4 |
| G6-31r | 1790 | 7616 | 1005 | 21.7 | 0.022 | 0.0538 | 0.0145 | 0.0013 | 0.0956 | 0.0105 | 0.0477 | 0.002 | 92.7 | 8.2 | 92.7 | 9.8 | 0.0 |
| G6-34r | 1797 | 7601 | 860 | 3.8 | 0.004 | 0.0538 | 0.0146 | 0.0013 | 0.0957 | 0.0107 | 0.0472 | 0.002 | 93.3 | 8.3 | 92.8 | 9.9 | -0.6 |
| G6-38r | 1742 | 7701 | 583 | 3.4 | 0.006 | 0.0538 | 0.0143 | 0.0012 | 0.0951 | 0.0100 | 0.0482 | 0.0020 | 91.4 | 7.7 | 92.3 | 9.3 | 0.9 |
| G6-40r | 1848 | 7855 | 698 | 10.0 | 0.014 | 0.0537 | 0.0141 | 0.0012 | 0.0925 | 0.0097 | 0.0476 | 0.0020 | 90.0 | 7.5 | 89.8 | 9.0 | -0.2 |
| Y32-17 | 1852 | 7781 | 616 | 6.0 | 0.010 | 0.0538 | 0.0146 | 0.0012 | 0.0962 | 0.0098 | 0.0477 | 0.0026 | 93.2 | 7.8 | 93.3 | 9.1 | 0.1 |
| Y32-38 | 1843 | 8050 | 430 | 4.0 | 0.009 | 0.0537 | 0.0135 | 0.0014 | 0.0871 | 0.0115 | 0.0471 | 0.002 | 86.7 | 9.2 | 84.8 | 10.7 | -2.3 |

Table 3 Kawakami et al.